Glacial to interglacial climate variability in the southeastern African subtropics (25- 20°S)

Annette Hahn[1], Enno Schefuß[1], Jeroen Groeneveld[1,2], Charlotte Miller[1*], Matthias Zabel[1],

[1]MARUM - Center for Marine Environmental Sciences, University of Bremen, Bremen, Germany

[2]Alfred Wegener Institute, Helmholtz Center for Polar and Marine Research, Potsdam, Germany

*Present address: Leeds Trinity University, Brownberrie Ln, Horsforth, Leeds, LS18 5HD, United Kingdom

Contact: ahahn@marum.de

Abstract

We present a continuous and well-resolved record of climatic variability for the past 100,000 yrs from a marine sediment core taken in Delagoa Bight, off southeastern Africa. In addition to providing a sea surface temperature reconstruction for the past ca. 100,000 yrs, this record also allows a high-resolution continental climatic reconstruction. Climate sensitive organic proxies, like the distribution and isotopic composition of plant-wax lipids as well as elemental indicators for fluvial input and weathering type provide information on climatic changes in the adjacent catchment areas (Incomati, Matola, and Lusutfu rivers). At the transition between glacials and interglacials, shifts in vegetation correlate with changes in sea surface temperature in the Agulhas current. The local hydrology, however, does not follow these orbital-paced shifts. Instead, precipitation patterns follow millennial scale variations with different forcing mechanisms in glacial versus interglacial climatic states. During glacials, southward displacement of the Intertropical Convergence Zone facilitates a transmission of northern hemispheric signals (e.g. Heinrich events) to the southern hemispheric subtropics. Furthermore, the southern hemispheric westerlies become a more direct source of precipitation as they shift northward over the study site, especially during Antarctic cold phases. During interglacials, the observed short-term hydrological variability is also a function of Antarctic climate variability, however, it is driven by the indirect influence of the southern hemispheric westerlies and the associated South African high-pressure cell blocking the South Indian Ocean Convergence Zone related precipitation. As a consequence of the interplay of these effects, small scale climatic zones exist. We propose a conceptual model describing latitudinal shifts of these zones along the southeastern African coast as tropical and temperate climate systems shift over glacial and interglacial cycles. The proposed

model explains some of the apparent contradictions between several paleoclimate records in the region.

Key words: Delagoa Bight; southern hemisphere westerlies; South Indian Ocean Convergence Zone; sea surface temperatures; hydrogen isotopes; carbon isotopes; elemental composition

1. Introduction

Despite the increasing number of southern African paleoclimate studies, large data gaps and unresolved debates remain. Controversies concern both the interpretation of the climate records as well as the contradictory major climate forcings that have been proposed for the region. In southeastern Africa, the main moisture source is the warm Indian Ocean (Tyson and Preston-Whyte, 2000), the mechanisms controlling the intensity and duration of the easterly rainfall over time remain, however, uncertain. Climate variations on glacial-interglacial timescales in southernmost Africa were reported to be directly forced by local (southern hemispheric) insolation (Partridge et al., 1997; Schefuß et al., 2011; Simon et al., 2015; Caley et al., 2018). Strong southern hemispheric summer insolation was hypothesized to cause wet climatic conditions along the east African coast due to a stronger atmospheric convection and an increase in the land/ocean temperature contrast, which results in higher moisture transport by the tropical easterlies. However, recent paleo-reconstructions suggested a synchrony with northern hemisphere climate signals, which are inversely correlated to southern hemispheric insolation (e.g. Truc et al., 2013). As a mechanism of transmitting the northern hemispheric signal to southern Africa, ocean circulation variability (Agulhas current strength; i.e. sea surface temperatures [SST]) has often been proposed (Biastoch et al., 1999; Reason and Rouault, 2005; Dupont et al., 2011; Tierney et al., 2008; Stager et al., 2011; Scott et al., 2012; Truc et al., 2013; Baker et al., 2017; Chase et al., 2017). In terms of vegetation shifts, atmospheric CO_2 variability and temperature have been suggested as major driving mechanisms over glacial-interglacial cycles (Dupont et al., 2019). Nowadays, eastern South Africa is not under the direct influence of the intertropical convergence zone (ITCZ) as its modern maximum southern extension is ca. 13-14°S (Gasse et al., 2008). However, the position of the ITCZ was more southerly during glacial periods (Nicholson and Flohn, 1980; Chiang et al., 2003; Chiang and Bitz, 2005), which may have allowed ITCZ shifts to reach much further south along the east African coast than today (c.f. Johnson et al., 2002; Schefuß et al., 2011; Ziegler et al., 2013; Simon et al., 2015). At the same time, the southern hemispheric westerlies (SHW), which presently influence only the southernmost tip of Africa, are hypothesized to have moved northward during glacial periods of increased south Atlantic sea ice extent (Anderson et al., 2009; Sigman et al., 2010; Miller et al., 2019b). As suggested by Miller et al., (2019b), in such a scenario the temperate systems may have brought winter moisture to the southeast African coast and/or blocked South Indian Ocean Convergence Zone (SIOCZ) related precipitation during the summer months. Regional studies integrating many of the available records have found that; i) several small-scale climatic dipoles exist due to the interaction of various driving mechanisms and that ii) the spatial extent of these climatic regions has varied considerably since the last Glacial (Chevalier et al., 2017, Chase et al., 2018; Miller et al., 2019b). Miller et al., (2019b) compile paleorecords along the southeastern African coast and propose a conceptual model of climatic variability during the Holocene. The authors describe three climatic zones; a *northern SRZ* where the climate is driven by local insolation, and *a central and eastern SRZ* and *southern South African* zone where climate is driven by shifts of the southern hemisphere westerlies, the South African high-pressure cell and the SIOCZ. Equatorward shifts of the southern hemisphere westerlies, the South African high-pressure cell and the SIOCZ result in humid conditions in the *southern South African zone*, whereas they cause arid conditions in the *central and eastern SRZ.* We analyze a marine core located within the *central and eastern SRZ* that offers a continuous high-resolution record of the past ca. 100,000 yrs allowing us to add to the existing conceptual models of southeastern African climate dynamics, and to gain an understanding of glacial climate mechanisms in the region. A combination of organic and inorganic geochemical proxies is used in order to decipher the hydrological processes on land, while foraminiferal shell geochemistry serves as a proxy for ocean circulation variability. With this approach we aim to decipher some of the discrepancies concerning the driving mechanisms of southeast African hydroclimate and vegetation shifts during the last glacial-interglacial cycle.

1.2 Regional setting

The coring site is located in an embayment on the southeastern African continental shelf called the Delagoa Bight (Fig. 1a). The southern directed Agulhas Current flows along the East African margin transporting warm and saline water from the tropical Indian Ocean to the tip of

Southern Africa (Zahn et al., 2012). The current system is structured into a series of large-scale (~200 km diameter) anti-cyclonic eddies occurring about 4 to 5 times per year (Quartly and Srokosz, 2004). As they pass the Delagoa Bight, these eddies, together with the Agulhas Current itself, drive the Delagoa Bight eddy; a topographically constrained cyclonic lee eddy at the coring location (Lutjeharms and Da Silva, 1988; Quartly and Srokosz, 2004). Although the coring site is located just west of the mouth of the major Limpopo river system, Schüürman et al., (2019) show that the inorganic material at our site most likely originates from three minor rivers, Incomati, Matola, and Lusutfu, that flow into the Indian Ocean further to the southwest. This is attributed to the eastward deflection of the Limpopo sediments by the Delagoa Bight eddy. The eddy appears to have been stable and strong enough to effectively constrain the drift of the Limpopo sediments eastwards over the late Pleistocene and Holocene (Schüürman et al., 2019). The three rivers, Incomati (also known as Komati), Matola (also known as Umbeluzi), and Lusutfu (also known as Maputo), have catchment areas of ca. 45 300 km^2, 6 600 km^2, and 22 700 km^2, respectively, comprising the coastal region and the eastern flank of the Drakensberg Mountains. Between the Drakensberg escarpment and the coast lies a N-S oriented low ridge, the Lebombo Mountains (400–800 m a.s.l.). The geological formations of this area are the Archaean Kaapvaal Craton, the Karoo Igneous Province, as well as the Quaternary deposits on the coastal plains (de Wit et al., 1992; Sweeney et al., 1994). Climatically these catchments are in the transition zone between tropical and subtropical climate; at the southern limit of the subtropical ridge between the southern Hadley and the Ferrel cell (Tyson and Preston-Whyte, 2000). The average annual temperature ranges from 16°C in the highlands to 24°C in the lowland area. (Kersberg, 1996). Rain (ca. 1,000 mm annually) falls mostly in summer (ca. 67 % of annual rainfall from November to March) (Xie and Arkin, 1997; Chase and Meadows, 2007). Although the ITCZ currently does not <u>directly</u> affect the region, it does induce latitudinal shifts in the SIOCZ, which can be considered as a southward extension of the ITCZ. When the ITCZ is in its southernmost (summer) position, tropical temperate troughs (TTTs), forming at the SIOCZ bring easterly rainfall from the Indian Ocean (Jury et al., 1993; Reason and Mulenga, 1999) (Fig 1b). During austral summer, a low-pressure cell dominates the Southern African interior, enabling tropical easterlies/TTT to bring rainfall to the region. This rainfall is suppressed during austral winter, when a subtropical high-pressure cell is located over southern Africa, (Fig. 1b). This high-pressure cell creates a blocking effect over the continent, which stops moisture advection inland over the majority of South Africa during winter (Dedekind et al., 2016). The winter rain that does fall (33 % of annual rainfall from April to October) is associated with extratropical cloud bands and thunderstorms linked to frontal systems that develop in the main SHW flow (between 40 °S and 50 °S). As the SHW shift northward during the winter, these frontal systems may become cut off and displaced equatorward as far north as 25°S (c.f. Baray et al., 2003; Mason and Jury, 1997) (Fig 1c). Associated with this climatological and topographic setting we find a vegetation in the Incomati, Matola, and Lusutfu catchment areas that consists mainly of coastal forests and mountain woodlands with savanna elements only in the northernmost parts of the catchment and sedges along the riverbanks and floodplains (see White, (1983) and Dupont et al., (2011) for a more detailed description of the vegetation biomes).

2 Material and methods

2.1 Sediments

Gravity core GeoB20616-1 (958 cm long) was retrieved from 25°35.395´S; 33°20.084´E on 15.02.2016 from a water depth of about 460 m. Shipboard sedimentological analysis showed a lithology of clayey silt with signs of slight bioturbation. The composition was observed as mainly clastic with occurrence of foraminifera and shell fragments (Zabel, 2016).

2.2 Oxygen isotopic composition of planktonic foraminifera

Stable oxygen isotopes values values of planktonic foraminifera (*G. ruber*, white variety, >150 µm) were measured in the interval between 395 and 935 cm at 10 cm resolution for age-modeling (Suppl.1). For each measurement, around eight shells of *G. ruber* were selected and analyzed at the MARUM – Center for Marine Environmental Sciences, University of Bremen, Germany using a ThermoFisher Scientific 253 plus gas isotope ratio mass spectrometer with Kiel IV automated carbonate preparation device. Data were calibrated against an in-house standard (Solnhofen limestone). The results are reported in permil (‰, parts per thousand) versus Vienna Peedee belemnite (VPDB). Standard deviation of in-house standard (Solnhofen limestone) $\delta^{18}O$ over the measurement period was 0.06 ‰.

2.3 Age model

Until the limit of radiocarbon dating the age model used in this study is based on 8 radiocarbon ages of *G. ruber*, one shell fragment and a bulk total organic carbon surface sample (see Table 1). The cleaning procedures as well as the Accelerator Mass Spectrometry (AMS) measurements were carried out in the Poznań Radiocarbon Laboratory, Poland. The modelled ocean average curve (Marine13) (Reimer et al., 2013) and a local marine ΔR of 121±16 ^{14}C yr (Maboya et al., 2017) were applied to calibrate the radiocarbon ages. To perform these calculations the Calib 7.1 software (Stuiver et al., 2019) was used. For flexible Bayesian age-depth modelling of the available ^{14}C dates, the software Bacon (Blaauw and Christen, 2011) (Fig. 2b) was used. The uncertainty of the radiocarbon dates is indicated in Table 1. The uncertainty of the Bacon model is indicated in Fig. 2b (grey lines). However, there is possibly an underestimation of the error in the age model around two periods of slow deposition in the interval from 15 to 6 ka BP and in the interval from 32 to 25 ka BP. The calibrated ^{14}C age of a shell fragment found in this interval (390cm) was used as a ^{14}C-tie-point (see Table 1), additionally 2 $\delta^{18}O$ tie-points were defined and an age model was calculated using the software AnalySeries (Paillard et al., 1996) (Fig. 2a). The age-depth model was extended by planktonic foraminifera $\delta^{18}O$ correlation using major $\delta^{18}O$ shifts in the LR04 stack as a reference (Lisiecki and Raymo, 2005) (Fig. 2a,b). With this low number of tie-points it is difficult to capture heterogeneity in the deposition rate, which must be considered when estimating the error of the age model. For the error estimation of $\delta^{18}O$ tie-points the mean resolution of the GeoB20616-1 $\delta^{18}O$ record and the reference curve around the tie-point depth and age (respectively) was taken into account as well as the absolute age error of the time-scale used for the reference record and a matching error visually estimated when defining tie-points. Figure 2b (grey lines) gives an estimate of the age model error. In this paper, we refer to median age estimations.

2.4 Foraminiferal Mg/Ca

Up to 20 specimens (> 150 µm) of *G. ruber* (white) (> 150 µm) were selected for Mg/Ca analysis (see Suppl.2). Foraminiferal tests were gently crushed prior to standard cleaning procedures for Mg/Ca in foraminifera (Barker et al., 2003). For clay and organic matter removal ultrasonic cleaning was alternated with washes in deionized water and methanol, an oxidizing step with 1 %-H_2O_2 buffered in 0.1M NaOH followed, which was then neutralized by deionized water washes.

A final weak acid leach with 0.001M QD HNO_3 was performed before dissolution in 0.5 mL 0.075 M QD HNO_3 and centrifugation for 10 min (6,000 rpm). The samples were diluted with Seralpur water before analysis with inductively coupled plasma optical emission spectrometry (Agilent Technologies, 700 Series with autosampler ASX-520 CETAC and micro-nebulizer) at MARUM, University of Bremen, Germany. Instrumental precision was monitored after every five samples using analysis of an in-house standard solution with a Mg/Ca of 2.93 mmol mol^{-1} (standard deviation of 0.020 mmol mol^{-1} or 0.67 %). A limestone standard (ECRM752-1, reported Mg/Ca of 3.75 mmol mol^{-1}) was analyzed to allow inter-laboratory comparison (Greaves et al., 2008; Groeneveld and Filipsson, 2013).

2.5 Organic geochemistry

Total lipid extracts (TLEs) were extracted from ca. 9-27 g of the freeze-dried, homogenized samples with a DIONEX Accelerated Solvent Extractor (ASE 200) at 100°C and at 1,000 psi for 5 minutes (repeated 3 times) using a dichloromethane (DCM):methanol (MeOH) (9:1, v/v) mixture. Squalane was added in a known amount to the samples as internal standard before extraction. Elemental sulphur was removed from the TLEs using copper turnings. After saponification by adding 6 % KOH in MeOH and extraction of the neutral fractions with hexane, the neutral fractions were split into hydrocarbon, ketone, and polar fractions using silica gel column chromatography (with a mesh size of 60 µm) and elution with hexane, DCM and DCM:MeOH (1:1), respectively. Subsequently elution of the hydrocarbon fractions with hexane over an $AgNO_3$-impregnated silica column yielded saturated hydrocarbon fractions. The concentrations of long-chain *n*-alkanes in the saturated hydrocarbon fractions were determined using a Thermo Fischer Scientific Focus gas-chromatograph (GC) with flame-ionization-detection (FID) equipped with a Restek Rxi 5ms column (30m x 0.25mm x 0.25µm). Quantities of individual *n*-alkanes were estimated by comparison with an external standard containing *n*-alkanes (C_{19}–C_{34}) at a known concentration. Replicate analyses of the external standard yielded a quantification uncertainty of <5 %. The carbon preference index (CPI) was calculated using the following equation:

$CPI = 0.5 * (\sum C_{odd27-33} / \sum C_{even26-32} + \sum C_{odd27-33} / \sum C_{even28-34})$ with C_x the amount of each homologue (Bray and Evans 1961).

The δD values of long-chain *n*-alkanes were measured using a Thermo Trace GC equipped with an Agilent DB-5MS (30m length, 0.25 mm ID, 1.00 µm film) coupled via a pyrolysis reactor (operated at 1420°C) to a Thermo Fisher MAT 253 isotope ratio mass spectrometer (GC/IR-MS). The δD values were calibrated against external H_2 reference gas. The H^{3+} factor was monitored daily and varied around 6.23 ± 0.04 ppm nA^{-1}. δD values are reported in permil (‰) versus Vienna Standard Mean Ocean Water (VSMOW). An *n*-alkane standard of 16 externally calibrated alkanes was measured every 6th measurement. Long-term precision and accuracy of the external alkane standard were 3 and <1 ‰, respectively. When *n*-alkane concentrations permitted, samples were run at least in duplicate. Precision and accuracy of the squalane internal standard were 2 and <1 ‰, respectively (n=41). Average precision of the *n*-C_{29} alkane in replicates was 4 ‰. The $\delta^{13}C$ values of the long-chain *n*-alkanes were measured using a Thermo Trace GC Ultra coupled to a Finnigan MAT 252 isotope ratio monitoring mass spectrometer via a combustion interface operated at 1,000°C. The $\delta^{13}C$ values were calibrated against external CO_2 reference gas. $\delta^{13}C$ values are reported in permil (‰) against Vienna Pee Dee Belemnite (VPDB). When concentrations permitted, samples were run at least in duplicate. Precision and accuracy of the squalane internal standard were 0.1 and 0.4 ‰, respectively (n=41). An external standard mixture was analyzed repeatedly every 6 runs and yielded a long-term mean standard deviation of 0.2 ‰ with a mean deviation of 0.1 ‰ from the reference values. Average precision of the *n*-C_{29} alkane in replicates was 0.3 ‰. We focus the discussion on the isotopic signals of the *n* -C_{31} alkane, as this compound is derived from grasses and trees present throughout the study area. Supplement 3 shows, however, that the *n* -C_{29} and *n* -C_{33} alkanes reveal similar trends.

2.6 Inorganic geochemistry

The elemental composition of all onshore and offshore samples was measured using a combination of high resolution (1 cm) semi-quantitative XRF scanning and lower (5 cm) resolution quantitative XRF measurements on discrete samples (see Suppl. 4). XRF core scanning (Avaatech XRF Scanner II at MARUM, University of Bremen) was performed with an excitation potential of 10 kV, a current of 250 mA, and 30 s counting time for Ca, Fe, K and Al. For discrete measurements on 110 dried and ground samples, a PANalytical Epsilon3-XL XRF spectrometer equipped with a rhodium tube, several filters, and a SSD5 detector was used. A calibration based on certified standard materials (e.g. GBW07309, GBW07316, and MAG-1) was used to quantify elemental counts (c.f. Govin et al., 2012).

3 Results and discussion

3.1 Proxy indicators

3.1.1 SST

The magnitude of temperature variability (from ca. 27°C during interglacials to ca. 24°C during glacials) in the GeoB20616-1 Mg/Ca SST record and the timing of changes (postglacial warming at ca. 17 ka BP) correspond to existing regional Mg/Ca SST records (c.f. Fig. 3; Bard et al., 1997; Levi et al., 2007; Wang et al., 2013). They do, however, not correspond to SST calculated from other indicators (i.e. $U^{K'}_{37}$, TEX^{86}) (e.g. Wang et al., 2013; Caley et al., 2011). These indicators show slightly different patterns, which may be attributed to a seasonal bias in the proxies (Wang et al., 2013). Wang et al., (2013) suggest that $U^{K'}_{37}$ SST reflects warm season SST mediated by changes in the Atlantic, whereas the *G. ruber* Mg/Ca SST indicator used in this study records cold season SST mediated by climate changes in the southern hemisphere.

3.1.2 Vegetation signatures

The $\delta^{13}C_{wax}$ record of core GeoB20616-1 shows average values of approximately -24‰ VPDB (c.f. Suppl. 3) and shifts from ca. -25 ‰ to ca. -24 ‰ (at 85 ka BP) and from -24 ‰ to – 25 ‰ (at ca. 10 ka BP). The stable carbon isotopic composition of plant waxes reflects discrimination between ^{12}C and ^{13}C during biosynthesis varying with vegetation type: C_4 plants have higher $\delta^{13}C$ values than C_3 plants (e.g., Collister et al., 1994; Herrmann et al., 2016). The average $\delta^{13}C$ value of the analyzed samples falls into the range between C_3 alkanes (around -35‰) and C_4 alkanes (around -20‰) (Garcin et al., 2014) indicating that the *n*-alkanes were derived from C_3 sources in the catchment such as mountain shrublands and coastal forests, as well as from C_4 sedges which grow along rivers and in the associated swamplands (c.f. Fig. 1a). There is no correlation (R^2=0.15) of $\delta^{13}C_{wax}$ variability and hydrological variability indicated by δD_{wax} (see section 3.1.3 Precipitation indicators for details on this proxy). We therefore suggest that the shifts we see in the $\delta^{13}C_{wax}$ werenot induced by a xeric/mesic adaptation of the same plant community. Instead, we imply that the shifts in the $\delta^{13}C_{wax}$ signal were related to shifts in the vegetation community. Palynological work on a nearby marine sediment core by Dupont et al. (2011) shows that large shifts in vegetation biomes are also observed in the Limpopo catchment which is directly adjacent to the Incomati, Matola and Lusutfu catchments (Fig. 1a). A comparison of the Dupont et al. (2011) palynological data (Fig. 3c) and the $\delta^{13}C_{wax}$ data at our site (Fig. 3a) shows a covariation of major shifts in vegetation and $\delta^{13}C_{wax}$. Although the similarities in the pattern of vegetation shifts detected in the nearby Limpopo river sediment core and at our study site suggest that large scale vegetation shifts took place in the region over glacial – interglacial transitions, this does not necessarily imply the mechanisms behind these trends are the same. Studies of the Limpopo sediment record (Dupont et al. 2011; Caley et al. 2018) reveal a $\delta^{13}C_{wax}$-enriched grassland vegetation for glacial intervals and an increase of woodland vegetation during well-developed interglacial periods, as is the case for MIS 5 and 1 (as opposed to MIS 3), reflected in lighter $\delta^{13}C_{wax}$ values. Caley et al., (2018) attribute the $\delta^{13}C_{wax}$-enrichment in Limpopo river sediments during glacials to an expansion of floodplains and the associated C_4 sedges, as well as discharge from the upper Limpopo catchment which reached well into the grassland interior of southern Africa (almost 1,000 km inland). The headwaters of the Incomati, Matola, and Lusutfu catchment areas, however, are in the Lebombo mountain range located within 200 km of the coast. They do not reach into the interior grassland biomes of South Africa. We therefore propose that in the Incomati, Matola, and Lusutfu catchment areas, the heavier $\delta^{13}C_{wax}$ values for the glacial MIS 4-2 interval reflect retreating forests and an expansion of drought tolerant C_4 plants (grasses) due to growing season aridity, whereas interglacial (MIS 1 and 5) lighter $\delta^{13}C_{wax}$ values reflect the formation of woodlands. Furthermore, sedge-dominated open swamps that fringed rivers during MIS 4-2 may have been replaced by gallery forests during MIS1 and 5 contributing to the glacial to interglacial $\delta^{13}C_{wax}$ depletion.

3.1.3 Precipitation indicators

Hydrogen isotope changes measured in plant waxes are related to the isotope composition of precipitation since hydrogen used for biosynthesis originates directly from the water taken up by the plants (Sessions et al., 1999). In tropical and subtropical areas, the isotopic composition of rainfall (δDp) mainly reflects the amount of precipitation - with δDp depletion indicating more rainfall (Dansgaard, 1964). Furthermore, rainfall δDp signatures may also become deuterium-depleted with altitude (ca. 10–15 ‰ per 1,000 m, Gonfiantini et al., (2001)). The δD values of leaf waxes in the three catchments are probably affected by both the amount as well as the altitude effect. Rainfall at higher altitudes takes place during times of generally increased rainfall, as it is high precipitation events that reach the interior. The altitude effect therefore enhances the δD depletion of the "amount effect". The K/Al ratio of the sediment is a less direct indicator of the precipitation regime: K/Al has been interpreted as an index between illite (K,H_3O) and kaolinite

($Al_2Si_2O_5(OH)_4$) giving an indication of the prevailing weathering regime as illite is a product of physical weathering whereas kaolinite is produced during chemical weathering (Clift et al., 2008; Dickson et al., 2010; Burnett et al., 2011). The Ca/Fe ratio is generally used as a proxy of marine (Ca) versus terrestrial (Fe) input to the core site and thus indicative of changes in terrestrial discharge by the river systems (Hebbeln and Cortés, 2001; Croudace et al., 2006; Rogerson et al., 2006; Rothwell and Rack, 2006; McGregor et al., 2009; Dickson et al., 2010; Nizou et al., 2010). The red/blue ratio of the sediment reflects sediment color nuance and increases with sediment lightness. In Geob20616-1 we interpret the reddish values as a more clastic deposition indicative of arid conditions whereas darker blueish colors may reflect clay and organic rich sediments preferentially deposited during humid phases (see also M123 cruise report Zabel, 2006). In the records of δD_{C31}, red/blue , K/Al and Ca/Fe similar patterns can be observed: They all display relatively high values (up to -144 ‰, 1.4; 12 and 0.25 respectively) in the intervals marked in red/yellow in Fig.4 and lower values (down to -160, 1.1, 1, and 0.2 respectively) in the intervals marked in blue/green in Fig. 4. We associate these variations with (respectively) decreasing (red/yellow) and increasing (blue/green) precipitation over the Incomati, Matola, and Lusutfu catchment areas. We note that the observed correlation, in particular for the inorganic proxies (K/Al and Ca/Fe), is relative rather than absolute in nature. This can be associated with the changing background conditions over glacial and interglacial cycles which may cause shifts in the elemental composition. We also note that of the four proxy indicators (δD_{C31}, red/blue, K/Al and Ca/Fe) only δD_{C31} can be considered as direct indicator of past precipitation change. Red/blue, K/Al and Ca/Fe depend to varying extents on precipitation, erosion and fluvial transport, whereas these factors do not necessarily vary in concert. For instance, erosion is not always directly linked to the amount of precipitation and vegetation density is often an additional and more important factor for erosion rates. Erosion rates can also increase substantially at times of rapid climatic and associated vegetation changes. Because the relationship between precipitation, erosion and riverine transport is not linear we base our precipitation reconstruction (i.e. the definition of the arid and wet intervals described in section 3.2 and colored-coded in Fig. 4) mainly on the δD_{C31} values. We consider the red/blue, K/Al and Ca/Fe values as supportive information; the relative correlation of the four proxies suggests that phases of increased precipitation are, for the most part, associated with an increase in erosion rates, chemical weathering and riverine transport. This underlines the reliability of our paleo-precipitation reconstruction.

3.2 Climatic patterns at different time scales

3.2.1 Orbital time scales

3.2.1.1. Sea surface temperatures and vegetation

Over the past 100,000 yrs the SST and $\delta^{13}C_{C31}$ values show a common trend of high SST and low $\delta^{13}C_{wax}$ values during interglacial MIS 5 and 1 and low SST and high $\delta^{13}C$ values during glacial MIS 4-2 (Fig. 3). Our data reveal an increase in SST of ca. 4°C from glacial to interglacial conditions. This correlation between SST and glacial-interglacial changes cycles is commonly found for this area (Caley et al., 2011; Dupont et al., 2011; Caley et al., 2018). On this glacial-interglacial time scale, variations in local SST are thought to be an important driver of hydroclimate in southeastern Africa (c.f. Dupont et al., 2011). During interglacials, warm SST within the Mozambique Channel and Agulhas Current induce an advection of moist air and higher rainfall in the east South African summer rainfall zone (e.g. Walker, 1990; Reason and Mulenga, 1999; Tyson and Preston-Whyte, 2000). The opposite effect is inferred for glacial periods (Dupont et al., 2011; Chevalier and Chase, 2015). The strong influence of western Indian Ocean surface temperatures on the summer precipitation in northern South Africa and southern Mozambique induces a tight coupling between vegetation dynamics in southeastern Africa and sea surface temperature variations in the Western Indian Ocean. This has been shown for several glacial – interglacial cycles in a palynological study offshore Limpopo River (core MD96-2048; Fig. 1a) by Dupont et al., (2011).

3.2.1.2. Hydrology over glacial-interglacial transitions

δD, XRF, and color data are indicators of catchment precipitation changes: decreases in red/blue, Ca/Fe, K/Al ratios and δD values indicate higher precipitation in the catchment, more fluvial discharge and higher chemical weathering rates (see section 3.1.3). Although there is much variability in the hydrological record of core GeoB20616-1, red/blue, Ca/Fe, K/Al ratios and δD values are surprisingly stable over glacial –interglacial transitions (mean δD value of MIS 1 and 5: -149 ‰ versus mean δD value of MIS 2-4: -150 ‰). It can be assumed that, during glacials, the rainfall from the main rain bearing systems (SIOCZ related tropical temperate troughs) was reduced due to generally lower land- and sea-surface temperatures and a weaker global hydrological cycle. However, a southward shift of the ITCZ during glacials as previously suggested

(Nicholson and Flohn, 1980; Johnson et al., 2002; Chiang et al., 2003; Chiang and Bitz, 2005; Schefuß et al., 2011) would have contributed to increased rainfall in the study area. It is unclear if the region would have been under the direct influence of the ITCZ during glacials or if southward shifts of the ITCZ entailed a southward shift of the SIOCZ and thus increased precipitation via the TTT. Furthermore, SHW related low pressure systems shifting northward to the Incomati, Matola and Lusutfu catchment areas during glacial conditions may have become a major additional precipitation source. The SHW northward shift of ca. 5° latitude is well documented (Chase and Meadows, 2007; Chevalier and Chase, 2015; Chase et al., 2017; Miller et al., 2019a). The possibility of more frequent SHW related low pressure systems bringing moisture to our study area during the LGM has previous been proposed by Scott et al., (2012) in the framework of a regional pollen review paper. It is also suggested by a modelling study showing an LGM scenario of drier summers and wetter winters for the southeastern African coast (Engelbrecht et al., 2019). During glacial periods, a reduced summer (SIOCZ related) rainfall amount and an increase in SHW related frontal systems as an additional winter precipitation source, possibly in combination with precipitation from a more southerly ITCZ, would translate to a relatively stable annual rainfall amount over glacial-interglacial transitions.

3.2.2 Millennial scale hydrological variability

3.2.2.1 During Interglacial MIS 5

During MIS 5 there are several prominent (ca. -10 **‰**) short-term (1-2 ka) decreases in the δD record, which are paralleled with decreases in Ca/Fe, K/Al and red/blue ratios (Fig. 4). We interpret these intervals (approximately 83-80 ka BP and 93-90 ka BP) as wet periods while intervals of high Ca/Fe, K/Al and red/blue ratios and δD values (approximately 97-95 ka BP, 87.5-85 ka BP and 77.5 ka BP) are interpreted as arid intervals (see section 3.1.2. for details on proxy interpretation). During the interglacial MIS 5, millennial scale increases in humidity correlate broadly to periods of warmth in the Antarctic ice core records termed AIM22 and AIM 21 (AIM: Antarctic isotope maxima) (see Fig. 4; EPICA members, 2010). During these Antarctic warm periods, sea ice, the circumpolar circulation and the SHW retracted. This is recorded by Southern Ocean diatom burial rates as well as paleoclimate archives at the southernmost tips of Africa and South America (Lamy et al., 2001; Anderson et al., 2009; Chase et al., 2009; Hahn et al 2016 and references therein; Zhao et al., 2016). It has been hypothesized that southward shifts of the SHW and the South African high-pressure cell, allow the SIOCZ and TTT to shift further south causing an increase in humidity in our study area. Miller et al., (2019b) suggest this mechanism for the region just south of our site (termed *eastern central zone*), which shows Holocene hydroclimatic shifts similar to those recorded in GeoB20616-1. Holocene arid events in this region are attributed to northward shifts of the SHW and the South African high-pressure cell which block the SIOCZ and TTT related moisture. These mechanisms are described in detail by Miller et al., 2019b and our data suggests that they were also active during earlier interglacial periods (e.g. MIS 5) (c.f. schematic model in Fig. 5a). Our current chronology suggests that southward SHW shifts during Antarctic warm periods caused the prominent humid phases during MIS 5 in the Incomati, Matola and Lusutfu catchment areas during the timeframes around 83-80 ka BP (AIM21) and 93-90 ka BP (AIM22). When our best age estimate is applied there is little correspondence between northern or southern insolation maxima and the MIS5 humid phases. In view of the chronological uncertainty in this early part of the record (beyond the ^{14}C dating limit), we cannot exclude that these humid phases are related to precessional variability, in the absence of ice interference, causing the division in MIS5a-e. However, in accordance with the conceptual model by Miller et al., (2019b) for the Holocene, we observe no local insolation control on climate at our study site. We suggest that the major shifts in the large-scale rain-bearing systems may override the local insolation forcing.

3.2.2.2. During MIS 4-2 glacial conditions

During the glacial periods MIS 2 and 4 and the less prominent interglacial MIS 3, the correlation between southeastern African humidity and Antarctic warm periods (AIM events) does not persist. In contrast; the first two prominent humid phases in MIS 4 (around 68-63 ka BP and 56 ka BP) as well as some of the following more short-term humid phases coincide with cold periods in the Antarctic ice core record (Fig.4). The general position of the SHW trajectories is suggested to have been located 5° in latitude further north during glacial periods (c.f. section *3.2.1.2. Hydrology over glacial-interglacial transitions*). The Incomati, Matola and Lusutfu catchment areas would therefore have been in the direct trajectory of the SHW related low pressure systems. Whilst northward shifts of the SHW and the South African high pressure cell during an interglacial cause aridity by blocking the SIOCZ and TTT (as suggested by Miller et al.,(2019b) and as described in section 3.2.2.1 for e.g. MIS 5), we suggest that during a glacial, additional northward shifts of the SHW (e.g. during Antarctic cold events) would have led to an increase in precipitation related to particularly strong direct influence of the SHW and the related low pressure cells (c.f. schematic model Fig 5b). Fig. 4 also shows a correlation between some of the humid phases during MIS 2-4 and Greenland cold phases i.e. Heinrich stadials. The timing of the wet phases at 68-63 ka, 56 ka, 44 ka, 37 ka, and 23 ka BP corresponds roughly to the following Heinrich stadials: HS6 (after 60 ka BP, Rasmussen et al., 2014); HS5a (56 ka BP, Chapman and Shackleton, 1999); HS5 (45 ka BP; Hemming 2004) and HS4 & HS2 (37 ka BP and 23 ka BP, Bond and Lotti, 1995). Wet phases in eastern Africa have previously been associated with Heinrich events (Caley et al., 2018; Dupont et al., 2011; Schefuß et al., 2011). It is well documented that during glacial conditions the large ice masses of the northern hemisphere displace the thermal equator southward (Nicholson and Flohn, 1980; Johnson et al., 2002; Chiang et al., 2003; Chiang and Bitz, 2005; Schefuß et al., 2011). It is therefore hypothesized that the ITCZ reached latitudes further south than its modern maximal extent causing the MIS 2-4 rainfall peaks. There is no notable “blocking” effect of the South African high-pressure cell during glacials (schematic model Fig. 5b). The transitions from cold “stadial” to warm “interstadial” conditions and back during MIS 2-4 are extremely rapid and short term. The sampling resolution and age – control of our record (especially prior to ca. 50 ka BP – the limit of ^{14}C dating) is not always sufficient for capturing these variations (e.g. HS4). The association of humid phases with a northward shifting SHW and/or southward shifting ITCZ is therefore not always clear and a combination of both may also be possible.

3.2.1.3 From the LGM to the Holocene

Relative to the prolonged arid phase during the late MIS 3/early MIS 2 (37-25 ka BP; c.f. Fig. 4), we observe a trend towards more humid conditions during the LGM (25 – 18 ka BP) marked by a decrease in Ca/Fe, K/Al, red/blue ratios and δD values. This is most likely due to the more frequent SHW-related low-pressure systems bringing moisture to our study area during the LGM and/or southward shifts of the ITCZ as discussed in section *3.2.1.2. Hydrology over glacial-interglacial transitions* (see also Fig. 5b). Our record shows a wettening trend after the Last Glacial Maximum and during the deglacial (from ca. 15 ka BP). Several paleoenvironmental records show a common humidity increase for this interval (Meadows 1988; Scott 1989; Norström et al., 2009). Chase et al.,(2017) attribute this to the invigoration of tropical systems with post-glacial warming. The wet conditions prevail until the early Holocene (ca. 8 ka BP). Similar observations of a ca. 15-8 ka BP wet phase have been made in the region (e.g. Norström et al., 2009; Neumann et al., 2010). For this early -Mid Holocene period, we infer from the leaf wax $\delta^{13}C$ values a shift from grassland to woodlands as described in section 3.2.1.1. and in Dupont et al. (2011). This may be related to the rainfall intensification as well as to the global temperature and CO_2 increase (c.f. Dupont et al., 2019). The early/Mid Holocene wet phase in our study region (*eastern central SRZ*) is described by Miller et al., 2019b and associated with a southward shift of the SHW and the South African high-pressure cell allowing for the SIOCZ related rain bearing systems (TTT) to shift southward over the region. The late Holocene (the last 5 kyrs) however, was an arid phase at our study cite as suggested by the precipitation indicators δD, Ca/Fe, K/Al and red/blue ratios. Several regional records (e.g. Mfabeni peatlands and the *eastern-central region*) show similar shifts; from a wet deglacial / Early Holocene (18-5 ka BP) to dry conditions thereafter (Chevalier et al., 2015; Miller et al., 2019a). Miller et al. (2019b) compile eastern African climate records and recognize a late Holocene tripole of increased humidity north of 20°S and south of 25°S and a contrasting aridity trend in the region in-between. Our catchment is located at the northernmost extent of this intermediate region; while we record an aridity trend in the Late Holocene, the adjacent Limpopo catchment just to the north received higher rainfall amounts during this time interval (Miller et al., 2019b). A northward shift in SHW with the South African high-pressure cell blocking the SIOCZ and TTT is a suggested mechanism for this late Holocene aridity (Miller et al., 2019b; also described in section 3.2.2.1). Likewise, Mason and Jury (1997) (based on a conceptual model by Tyson (1984)) suggest that northward shifting SHW induce rain-bearing low pressure cells to shift away from the eastern African coast towards Madagascar. During the Late Holocene the modern climatic situation of the study area was established: during the summer months the SHW and the South African high-pressure cell are in their southernmost position allowing the SIOCZ related TTT to bring rainfall to the region (66 % of annual precipitation). During the winter months the SHW and the South African high-pressure cell shift northward. In this constellation the SIOCZ and TTT influence are blocked by the South African high-pressure cell, however low-pressure cells may become cut from the main SHW flow bringing winter rainfall to the area (33 % of annual precipitation) as described in section 1.2.

Conclusions

Using the organic and inorganic geochemical properties of sediment core GeoB20616-1 from the Delagoa Bight we were able to reconstruct the vegetation changes and rainfall patterns in the Incomati, Matola and Lusutfu catchments as well as SST trends of the Agulhas waters for the past ca. 100,000 yrs offshore southeastern Africa. Our reconstructions underline the existing dipoles or tripoles in southeastern African climate: although the glacial-interglacial variability at our site resembles that observed in the adjacent Limpopo river catchment, the Holocene hydrological trends are exactly inverted in these neighboring catchments. Small-scale climatic zones have been previously described for the region (c.f. Scott et al., 2012; Chevalier and Chase, 2015; Miller et al., 2019b) and each zone has been attributed to a climatic driving mechanism. Our data provide insights into the spatial shifts of these zones as fundamental shifts in the major climate systems occurred over glacial-interglacial cycles. In accordance with Miller et al., (2019b) we identify displacements of the SHW as the main hydro-climate driver during the Holocene in our study area (termed *central and eastern zone*). The main trajectories of the SHW related disturbances remain so far south during the Holocene, that they rarely deliver direct rainfall to the study area. Instead, northward shifts of the SHW and the South African high-pressure cell block the SIOCZ and thus TTT related rainfalls over the region (Fig. 5a). In this manner latitudinal SHW shifts influence the local rainfall indirectly. Our study not only confirms the Miller et al. (2019 b) conceptual model for the Holocene, but also finds the same mechanisms to be active during MIS5. Similar to Miller et al. (2019b) we find an absence of insolation forcing in our study area. We suggest that at these latitudes local insolation as a climatic forcing mechanism is overridden by shifts in the major rain-bearing systems. We conclude that during interglacials regional wet phases are induced by southward shifting westerlies (related to Antarctic warming trends) allowing for the influence of the SIOCZ related TTT. During glacial periods, however, we observe an inverted relationship between Antarctic warm events and regional humidity, and an additional correlation of several humid intervals with extreme northern hemispheric cold events (HS). This suggests that the mechanisms driving the millennial scale hydrological variability during glacials are not the same as during interglacials. We attribute this to the global reorganization of climate systems during the glacial as the large ice masses at both poles induce a southward shift of the thermal equator and the ITCZ as well as a northward shift of the SHW. Our study site is located at the interface of these "compressed" climate systems. As a result, during full glacial conditions, the region may have received precipitation both from SHW related disturbances as well as from SIOCZ related TTT (Fig. 5b). In this "compressed" state the northward shifts of the SHW and the South African high pressure no longer have the net effect of blocking SIOCZ related precipitation; as this is compensated by the increase in winter rains. Overall humidity therefore shows no considerable decrease during MIS 2-4. Nevertheless, a shift in vegetation from woodland to grasslands takes place during glacials; we attribute this to a reduced growing-season (summer) precipitation, probably in combination with low temperatures and atmospheric CO_2. Our study shows that these mechanisms are active in a spatially very restrained area resulting in small-scale variability. These small-scale climatic dipoles or tripoles make the southeastern African coastal area especially sensitive to shifts in the global climatic system.

Acknowledgments

This work was financially supported by Bundesministerium für Bildung und Forschung (BMBF, Bonn, Germany) within the projects "Regional Archives for Integrated Investigation (RAiN)," project number: 03G0840A and "Tracing Human and Climate impacts in South Africa (TRACES)" project number: 03F0798C. The captain, crew, and scientists of the Meteor M123 cruise are acknowledged for facilitating the recovery of the studied material. This study would not have been possible without the MARUM—Center for Marine Environmental Sciences, University of Bremen, Germany and the laboratory help of Dr. Henning Kuhnert, Ralph Kreutz and Silvana Pape. In particular, we thank the GeoB Core Repository at the MARUM and Pangaea (www.pangaea.de) for archiving the sediments and the data used in this paper. Thanks to all RAiN members as well as Stephan Woodborne and the anonymous reviewer of this manuscript for critical comments and helpful advice.

Captions

Fig. 1 A: Modern vegetation of southern Africa and the Incomati, Matola and Lusutfu catchments (after White 1983) and annual SST over the Indian Ocean (Locarnini et al., 2013). Grey arrows represent the main easterly transport of moisture from the warm Indian Ocean. The Mozambique current (MC), Agulhas current (AC), and counter current (cc) forming a coastal eddy are shown in black. Sites mentioned in the discussion are numbered as: 1) Wonderkrater (Truc et al., 2013); 2) Braamhoek (Norström et al., 2009); 3) Mfabeni (Miller et al., 2019a); 4) MD96-2048 (Dupont et al., 2011; Caley et al., 2011, 2018); 5) GeoB20610-1 (Miller et al., 2019b); 6) GIK16160-3 (Wang et al., 2013); 7) MD79-257 (Bard et al., 1997; Sonzogni et al., 1998; Levi et al., 2007); 8) GeoB9307-3 (Schefuß et al., 2011). B: Map of South Africa in austral summer showing the shematic postion of the low-pressure system, the ITCZ (Intertopical Convergence Zone), the SIOCZ (South Indian Ocean convergence zone) and related rain bearing TTT (tropical temperate troughs). C: Map of South Africa in austral winter showing the shematic postion of the high-pressure system, the weaker TTT (tropical temperate troughs) and the frontal systems associated with the northward shifted SHW (southern hemispheric westerlies).

Fig. 2 Reference curves and age–depth model of core GeoB20616-1. A: LR04 benthic foraminifera $\delta^{18}O$ stack (Lisiecki and Raymo, 2005) (black) compared to GeoB20616-1 (red) *G. ruber* foraminifera $\delta^{18}O$ with indicated tie points. B: Age-depth model based on Bacon v. 2.2 (Blaauw and Christen, 2011; green) and $\delta^{18}O$ correlation (blue). Blue circles in panel B represent the positions of calibrated ^{14}C ages whereas blue circles indicate $\delta^{18}O$ tie points. Grey lines indicate uncertainty.

Fig. 3 Climatic patterns at orbital time scales recorded in GeoB20616-1. Panel a) shows down-core $\delta\ ^{13}C$ values of the C_{31} *n*- alkane in ‰ VPDB of GeoB20616-1 as indicators for shifts in vegetation type (C_3 vs. C_4). Panel b) shows SST (sea surface temperatures) recorded by *G. ruber* Mg/Ca (black line) in GeoB20616-1 as well as offshore Limpopo River (core MD96-2048) SST calculated from TEX_{86} (dashed line) and from $U^{K'}{}_{37}$ (grey line) (Caley et al., 2011). Panel c) shows Limpopo vegetation endmember EM2 from Dupont et al. (2011). The diamonds indicate C^{14} dates (red) and $\delta^{18}O$ tie points (orange).

Fig. 4 Millennial scale hydrological variability recorded in core GeoB20616-1. Organic and inorganic down-core geochemistry (c-f: δD, red/blue, K/Al and Ca/Fe) of GeoB20616-1 as indicators for weathering type, fluvial input and aridity. Intervals identified as wet using these indicators are marked in blue or green, while dry phases are marked in red or yellow. Wet intervals marked in green are associated with southward shifts of the SHW (southern hemispheric westerlies) and the South African high-pressure cell allowing for the SIOCZ (South Indian Ocean convergence zone) and related rain bearing TTT (tropical temperate troughs) to move over the study area during interglacials. In turn, wet intervals marked in blue are associated with northward shifts of the SHW and/or southward shifts of the ITCZ during glacials. Arid phases during interglacials (marked in yellow) are related to northward shifts of the SHW as this induces the moisture-blocking effect of the South African high-pressure cell over the region. During glacials, however, southward shifts of the SHW are often associated with arid phases (marked in red) as the rain-bearing systems related to the SHW move south. Transitional intervals between arid and wet intervals are not colored. XRF scanning data is marked as a line, whereas discrete XRF measurements are represented by points. Panel c represents the δD of the C_{31} *n* alkane in the unit ‰ VSMOW. For comparative purposes local insolation (Laskar, 2011) as well as Arctic and Antarctic ice core d^{18}O records are plotted (NGRIP members, 2004; EPICA members, 2010). The most prominent AIM (Antarctic isotope maxima) and HS (Heinrich Stadial) events are named. The diamonds indicate C^{14} dates (red) and δ^{18}O tie points (orange).

Fig. 5 Conceptual model of precipitation shifts during glacial vs. interglacial (present conditions) intervals. The blue shaded boxes indicate the locations of the major regional rain-bearing systems: i) the TTT (tropical temperate troughs) moisture shifting with the SIOCZ (south Indian Ocean convergence zone) and bearing summer rain (therefore marked as SR) ii) the low-pressure systems related to the SHW (southern hemispheric westerlies), bringing mainly winter rain (therefore marked as WR). The orange shaded box marks South African high-pressure cell (HPC) shifting with the SHW. The HPC blocks SIOCZ and TTT related moisture and therefore causes aridity. The arrows mark the millennial scale variability of the position of these systems over the study area which is marked by a star. Please note that the millennial scale variations that the region experiences differ in the interglacial state (box A) and the glacial state (box B) since the organization of the major climatic systems (marked in red) is different ("decompressed" vs "compressed"). The conceptualization for interglacial states presented in box A is based on a schematic model by (Miller et al., 2019b). In this "decompressed" state latitudinal shifts of the SHW indirectly control precipitation at our study site via the moisture blocking effect of the South African HPC: southward shifts of the SHW and HPC allow the SIOCZ related TTT to bring SR to our site, whereas northward movements block this SR moisture (Miller et al., 2019b). During the "compressed" glacial state (box B) the SHW related WR reaches much further north, directly influencing the study site. The SR, in turn is shifted southward and an HPC blocking effect is not noted at our site.

Table. 1 AMS radiocarbon analyses of material from core GeoB20616-1. The modelled ocean average curve (Marine13) (Reimer et al., 2013) was used for calibration and a local ΔR of 121±16 ^{14}C yr (Maboya et al., 2017) was applied. The ages were calibrated with Calib 7.1 software (Stuiver et al., 2019)

Supplement 1 GeoB20616-1 Oxygen and carbon isotopic composition of planktonic foraminifera (*G.ruber*).

Supplement 2 GeoB20616-1 downcore sea surface temperatures (SST) calculated following Lea et al., 2003 using Mg/Ca analysed on the planktonic foraminifer *G. ruber* (in mmol/mol).

Supplement 3 GeoB20616-1 organic geochemical down-core data. *n*-alkane isotopic composition and distribution descriptive parameters averaged. The elevated CPI values ranging from 3.8 to 14 indicate that the *n*-alkanes within the terrestrial and marine samples were likely derived from non-degraded, terrestrial, higher plant material (Eglinton & Hamilton, 1967). We focus the discussion on the isotopic signals of the *n*-C_{31} alkane but note that the *n*-C_{29} and *n*-C_{33} alkanes reveal similar trends.

Supplement 4 GeoB20616-1 inorganic geochemical down-core data from discrete XRF measurements.

Contributor Roles

Annette Hahn: conceptualization, investigation, analysis, visualisation, writing
Enno Schefuß: funding acquisition, conceptualization, investigation, review & editing
Jeroen Groeneveld: analysis, interpretation, methodology, review & editing
Charlotte Miller: analysis, interpretation, review & editing
Matthias Zabel: funding acquisition, project administration, conceptualization, investigation, review & editing

Sample and data availability

Samples and data are respectively archived at the GeoB Core Repository and Pangaea (www.pangaea.de) both located at MARUM, University of Bremen.

References

Anderson, R. F., Ali, S., Bradtmiller, L. I., Nielsen, S. H. H., Fleisher, M. Q., Anderson, B. E., and Burckle, L. H.: Wind-Driven Upwelling in the Southern Ocean and the Deglacial Rise in Atmospheric CO_2, Science, 323, 1443-1448, https:doi.org/10.1126/science.1167441, 2009.

Baker, A., Pedentchouk, N., Routh, J., Roychoudhury, A. N.: Climatic variability in peatlands (South Africa) since the late Pleistocene, Quat. Sci. Rev., 160: 57-66, 2017.

Baray, J. L., Baldy, S., Diab, R. D., Cammas, J. P.: Dynamical study of a tropical cut-off low over South Africa, and its impact on tropospheric ozone, Atmos. Environ., 37(11), 1475-1488, 2003.

Bard, E., Rostek, F., Sonzogni, C.: Interhemispheric synchrony of the last deglaciation inferred from alkenone palaeothermometry, Nature, 385(6618), 707, 1997.

Barker, S., Greaves, M., and Elderfield, H.: A study of cleaning procedures used for foraminiferal Mg/Ca paleothermometry, Geochemistry, Geophysics, Geosystems, 4, 10.1029/2003gc000559, 2003.

Biastoch, A., Reason, C. J. C., Lutjeharms, J. R. E., Boebel, O.: The importance of flow in the Mozambique Channel to seasonality in the greater Agulhas Current system, Geophys. Res. Lett., 26, 3321-3324, 1999.

Blaauw, M., Christen, J. A.: Flexible paleoclimate age-depth models using an autoregressive gamma process, Bayesian analysis, 6(3), 457-474, 2011.

Bond, G. C. and Lotti, R.: Iceberg Discharges into the North Atlantic on Millennial Time Scales During the Last Glaciation, Science 267(5200), 1005-1010, 1995.

Burnett, A. P., Soreghan, M. J., Scholz, C. A., Brown, E. T.: Tropical East African climate change and its relation to global climate: a record from Lake Tanganyika, Tropical East Africa, over the past 90+ kyr, Palaeogeogr. Palaeoclimatol. Palaeoecol., 303(1-4), 155-167, 2011.

Caley, T., Extier, T., Collins, J. A., Schefuß, E., Dupont, L., Malaizé, B., Rossignol, L., Souron, A., McClymont, E. L., and Jimenez-Espejo, F. J.: A two-million-year-long hydroclimatic context for hominin evolution in southeastern Africa, Nature, 1, 2018.

Caley, T., Malaizé, B., Revel, M., Ducassou, E., Wainer, K., Ibrahim, M., Shoeaib, D., Migeon, S., and Marieu, V.: Orbital timing of the Indian, East Asian and African boreal monsoons and the concept of a 'global monsoon', Quat. Sci. Rev., 30, 3705-3715, 2011.

Chapman, M. R. and Shackleton N. J.: Global ice-volume fluctuations, North Atlantic ice-rafting events, and deep-ocean circulation changes between 130 and 70 ka, Geology, 27(9), 795-798, 1999.

Chase, B. M., Chevalier, M., Boom, A., Carr, A. S.: The dynamic relationship between temperate and tropical circulation systems across South Africa since the last glacial maximum, Quat. Sci. Rev., 174, 54-62, 2017.

Chase, B. M., Faith, J. T., Mackay, A., Chevalier, M., Carr, A. S., Boom, A., Lim, S., and Reimer, P. J.: Climatic controls on Later Stone Age human adaptation in Africa's southern Cape, J. Hum. Evol., 114, 35-44, 2018.

Chase, B. M., Meadows, M. E.: Late Quaternary dynamics of southern Africa's winter rainfall zone, Earth Sci. Rev., 84(3-4), 103-138, 2007.

Chase, B., Meadows, M., Scott, L., Thomas, D., Marais, E., Sealy, J., and Reimer, P.: A record of rapid Holocene climate change preserved in hyrax middens from southwestern Africa, Geology, 37, 703-706, 2009.

Chevalier, M., Brewer, S., Chase, B. M.: Qualitative assessment of PMIP3 rainfall simulations across the eastern African monsoon domains during the mid-Holocene and the Last Glacial Maximum, Quat. Sci. Rev., 156, 107-120, 2017.

Chevalier, M., Chase, B. M.: Southeast African records reveal a coherent shift from high- to low-latitude forcing mechanisms along the east African margin across last glacial–interglacial transition, Quat. Sci. Rev., 125, 117-130, 2015.

Chiang, J. C. H., Biasutti, M., Battisti, D. S.: Sensitivity of the Atlantic Intertropical Convergence Zone to Last Glacial Maximum boundary conditions, Paleoceanogr., 18(4), 2003.

Chiang, J. C. H., Bitz, C. M.: Influence of high latitude ice cover on the marine Intertropical Convergence Zone, Clim. Dyn., 25(5), 477-496, 2005.

Clift, P. D., Hodges, K. V., Heslop, D., Hannigan, R., Van Long, H., and Calves, G.: Correlation of Himalayan exhumation rates and Asian monsoon intensity, Nat. Geosci., 1, 875, 2008.

Croudace, I. W., Rindby, A., Rothwell, R. G.: ITRAX: Description and evaluation of a new multi-function X-ray core scanner, Geol. Soc. Spec. Publ., London, 267(1), 51-63, 2006.

Dansgaard, W.: Stable isotopes in precipitation, Tellus, 16(4), 436-468, 1964.

De Wit, M. J., De Ronde, C. E. J., Tredoux, M., Roering, C., Hart, R. J., Armstrong, R. A., Green, R. W. E., Peberdy, E., and Hart, R. A.: Formation of an Archaean continent, Nature, 357, 553-562, https:doi.org /10.1038/357553a0, 1992.

Dickson, A., Leng, M., Maslin, M., Röhl, U.: Oceanic, atmospheric and ice-sheet forcing of Southeast Atlantic Ocean productivity and South African monsoon intensity during MIS-12 to 10, Quat. Sci. Rev., 29, 3936-3947, 2010.

Dupont, L. M., Caley, T., Kim, J. H., Castañeda, I., Malaizé, B., and Giraudeau, J.: Glacial-interglacial vegetation dynamics in Southeastern Africa coupled to sea surface temperature variations in the Western Indian Ocean, Clim. Past, 7, 1209-1224, https:doi.org /10.5194/cp-7-1209-2011, 2011.

Dupont, L. M., Caley, T., and Castañeda, I. S.: Effects of atmospheric CO2 variability of the past 800kyr on the biomes of southeast Africa, Clim. Past, 15, 1083-1097, 10.5194/cp-15-1083-2019, 2019.

Eglinton, G., and Hamilton, R. J.: Leaf epicuticular waxes, Science, 156, 1322-1335, 1967.

Engelbrecht, F. A., Marean, C. W., Cowling, R. M., Engelbrecht, C. J., Neumann, F. H., Scott, L., Nkoana, R., O'Neal, D., Fisher, E., Shook, E., Franklin, J., Thatcher, M., McGregor, J. L., Van der Merwe, J., Dedekind, Z., and Difford, M.: Downscaling Last Glacial Maximum climate over southern Africa, Quaternary Science Reviews, 226, 105879, https://doi.org/10.1016/j.quascirev.2019.105879, 2019.

EPICA Members: Stable oxygen isotopes of ice core EDML, PANGAEA, 2010

Gasse, F., Chalié, F., Vincens, A., Williams M. A. J., and Williamson D.: Climatic patterns in equatorial and southern Africa from 30,000 to 10,000 years ago reconstructed from terrestrial and near-shore proxy data, Quat. Sci. Rev., 27(25), 2316-2340, 2008.

Gonfiantini, R., Roche, M.-A., Olivry, J.-C., Fontes, J.-C., Zuppi, G. M.: The altitude effect on the isotopic composition of tropical rains, Chem. Geol., 181(1–4), 147-167, 2001.

Govin, A., Holzwarth, U., Heslop, D., Ford Keeling, L., Zabel, M., Mulitza, S., Collins, J. A., and Chiessi, C. M.: Distribution of major elements in Atlantic surface sediments (36°N–49°S): Imprint of terrigenous input and continental weathering, Geochem. Geophys. Geosys., 13, https:doi.org /Q01013, 10.1029/2011GC003785, 2012.

Greaves, M., Caillon, N., Rebaubier, H., Bartoli, G., Bohaty, S., Cacho, I., Clarke, L., Cooper, M., Daunt, C., and Delaney, M.: Interlaboratory comparison study of calibration standards for foraminiferal Mg/Ca thermometry, Geochem. Geophys. Geosys., 9, 2008.

Groeneveld, J., Filipsson, H.: Mg/Ca and Mn/Ca ratios in benthic foraminifera: the potential to reconstruct past variations in temperature and hypoxia in shelf regions, Biogeosci., 10(7), 5125-5138, 2013.

Hahn, A., Schefuß, E., Andò, S., Cawthra, H. C., Frenzel, P., Kugel, M., Meschner, S., Mollenhauer, G., and Zabel, M.: Linking catchment hydrology and ocean circulation in Late Holocene southernmost Africa, Climate of the Past Discussions. doi, 10, 2016.Hebbeln, D., Cortés, J.: Sedimentation in a tropical fjord: Golfo Dulce, Costa Rica, Geo-Marine Letters, 20(3), 142-148, 2001.

Hemming, S. R.: Heinrich events: Massive late Pleistocene detritus layers of the North Atlantic and their global climate imprint, Rev. Geophys., 42, https:doi.org /10.1029/2003RG000128, 2004.

Johnson, T. C., Brown, E. T., McManus, J., Barry, S., Barker, P., and Gasse, F.: A high-resolution paleoclimate record spanning the past 25,000 years in southern East Africa, Science, 296, 113-132, https:doi.org /10.1126/science.1070057, 2002.

Jury, M. R., Valentine, H. R., Lutjeharms, J. R. E.: Influence of the Agulhas Current on Summer Rainfall along the Southeast Coast of South Africa, J. Appl. Meteorol., 32(7), 1282-1287, 1993.

Kersberg, H.: Vegetationsgeographie, Südafrika (Mosambik, Swasiland, Republik Südafrika), Gebrüder Borntraeger, 1996.

Lamy, F., Hebbeln, D., Röhl, U., and Wefer, G.: Holocene rainfall variability in southern Chile: a marine record of latitudinal shifts of the Southern Westerlies, Earth and Planetary Science Letters, 185, 369-382, 2001.

Lea, D. W., Pak, D. K., Peterson, L. C., and Hughen, K. A.: Synchroneity of tropical and high-latitude Atlantic temperatures over the last glacial termination, science, 301, 1361-1364, 2003.

Levi, C., Labeyrie, L., Bassinot, F., Guichard, F., Cortijo, E., Waelbroeck, C., Caillon, N., Duprat, J., de Garidel-Thoron, T., and Elderfield, H.: Low-latitude hydrological cycle and rapid climate changes during the last deglaciation, Geochem. Geophys. Geosyst., 8, 2007.

Lisiecki, L. E., Raymo, M. E.: A Pliocene-Pleistocene stack of 57 globally distributed benthic $\delta^{18}O$ records, Paleoceanogr., 20(1), 2005.

Locarnini, R. A., Mishonov, A. V., Antonov, J. I., Boyer, T. P., Garcia, H. E., Baranova, O. K., Zweng, M. M., Paver, C. R., Reagan, J. R., Johnson, D. R., Hamilton, M., Seidov, D., and Levitus, S.: World ocean atlas 2013, Volume 1, Temperature, http://doi.org/10.7289/V55X26VD, 2013.

Lutjeharms, J. R. E., and Da Silva, A. J., 1988, The Delagoa Bight eddy: Deep Sea Research Part A.

Magill, C.R., Ashley, G.M., Freeman, K.H., 2013. Ecosystem variability and early human habitats in eastern Africa. Proceedings of the National Academy of Sciences 110, 1167-1174. Oceanographic Research Papers, v. 35, p. 619-634.

Maboya, L., Meadows, M., Reimer, P., Haberzettl, T.: Marine reservoir correction ΔAR, for south and east coasts of South Africa, 21st Biennial Conference of the South African Society of Quaternary Research, Johannesburg, 3–7 April 2017, 25, 2017.

Mason, S., Jury, M.: Climatic variability and change over southern Africa: a reflection on underlying processes, Prog. Phys. Geogr., 21(1), 23-50, 1997.

McGregor, H. V., Dupont, L., Stuut, J.-B. W., Kuhlmann, H.: Vegetation change, goats, and religion: a 2,000-year history of land use in southern Morocco, Quat. Sci. Rev., 28(15), 1434-1448, 2009.

Miller, C., Finch, J., Hill, T., Peterse, F., Humphries, M., Zabel, M., and Schefuß, E.: Late Quaternary climate variability at Mfabeni peatland, eastern South Africa, Clim. Past, 15, 1153-1170, https:doi.org /10.5194/cp-15-1153-2019, 2019.

Miller, C., Hahn, A., Zabel, M., Schefuß, E.: Mid- and low latitude effects on eastern South African rainfall over the last 7 thousand years , Quat. Sci. Rev., 2019.

Neumann, F. H., Scott, L., Bousman, C. B., and Van As, L.: A Holocene sequence of vegetation change at Lake Eteza, coastal KwaZulu-Natal, South Africa, Rev. Palaeobot. Palynol., 162, 39-53, https://doi.org/10.1016/j.revpalbo.2010.05.001, 2010.

NGRIP members,: High-resolution record of Northern Hemisphere climate extending into the last interglacial period, Nature 431(7005), 147-151, 2004.

Nicholson, S. E., Flohn, H.: African environmental and climatic changes and the general atmospheric circulation in late Pleistocene and Holocene, Clim. Change, 2(4), 313-348, 1980.

Nizou, J., Hanebuth, T. J. J., and Vogt, C.: Deciphering signals of late Holocene fluvial and aeolian supply from a shelf sediment depocenter off Senegal (north-west Africa), J. Quat. Sci., 26, 411-421, https:doi.org /10.1002/jqs.1467, 2010.

Norström, E., Scott, L., Partridge, T., Risberg, J., and Holmgren, K.: Reconstruction of environmental and climate changes at Braamhoek wetland, eastern escarpment South Africa, during the last 16,000 years with emphasis on the Pleistocene–Holocene transition, Palaeogeogr. Palaeoclimatol. Palaeoecol., 271, 240-258, 2009.

Paillard, D., Labeyrie, L., and Yiou, P.: Macintosh program performs time‐series analysis, Eos, Transactions American Geophysical Union, 77, 379-379, 1996.

Partridge, T. C., Demenocal, P. B., Lorentz, S. A., Paiker, M. J., Vogel, J. C.: Orbital forcing of climate over South Africa: A 200,000-year rainfall record from the pretoria saltpan, Quat. Sci. Rev., 16(10), 1125-1133, 1997.

Quartly, G. D., and Srokosz, M. A., 2004, Eddies in the southern Mozambique Channel: Deep Sea

Research Part II: Topical Studies in Oceanography, v. 51, p. 69-83.Rasmussen, S. O., Bigler, M., Blockley, S. P., Blunier, T., Buchardt, S. L., Clausen, H. B., Cvijanovic, I., Dahl-Jensen, D., Johnsen, S. J., Fischer, H., Gkinis, V., Guillevic, M., Hoek, W. Z., Lowe, J. J., Pedro, J. B., Popp, T., Seierstad, I. K., Steffensen, J. P., Svensson, A. M., Vallelonga, P., Vinther, B. M., Walker, M. J. C., Wheatley, J. J., and Winstrup, M.: A stratigraphic framework for abrupt climatic changes during the Last Glacial period based on three synchronized Greenland ice-core records: refining and extending the INTIMATE event stratigraphy, Quat. Sci. Rev., 106, 14-28, https://doi.org/10.1016/j.quascirev.2014.09.007, 2014.

Reason, C., Mulenga, H.: Relationships between South African rainfall and SST anomalies in the southwest Indian Ocean, Int. J. Climatol., 19, 1651-1673, 1999.

Reason, C., Rouault, M.: Links between the Antarctic Oscillation and winter rainfall over western South Africa, Geophys. Res. Lett., 32(7), 2005.

Reimer, P. J., Bard, E., Bayliss, A., Beck, J. W., Blackwell, P. G., Ramsey, C. B., Buck, C. E., Cheng, H., Edwards, R. L., and Friedrich, M.: IntCal13 and Marine13 radiocarbon age calibration curves 0–50,000 years cal BP, Radiocarbon, 55, 1869-1887, 2013.

Rogerson, M., Rohling, E., Weaver, P.: Promotion of meridional overturning by Mediterranean-derived salt during the last deglaciation, Paleoceanogr., 21(4), 2006.

Rothwell, R. G., Rack, F. R.: New techniques in sediment core analysis: an introduction, Geol. Soc. Spec. Publ., 267(1), 1-29, https://doi.org/10.1144/GSL.SP.2006.267.01.01, 2006.

Schefuß, E., Kuhlmann, H., Mollenhauer, G., Prange, M., Patzold, J.: Forcing of wet phases in southeast Africa over the past 17,000 years, Nature, 480(7378), 509-12, 2011.

Schüürman, J., Hahn, A., Zabel, M.: In search of sediment deposits from the Limpopo (Delagoa Bight, southern Africa): Deciphering the catchment provenance of coastal sediments, Sediment. Geol., 380, 94-104, 2019.

Scott, L., Neumann, F. H., Brook, G. A., Bousman, C. B., Norström, E., and Metwally, A. A.: Terrestrial fossil-pollen evidence of climate change during the last 26 thousand years in Southern Africa, Quat. Sci. Rev., 32, 100-118, https:doi.org/10.1016/j.quascirev.2011.11.010, 2012.

Sessions, A. L., Burgoyne, T. W., Schimmelmann, A., Hayes, J. M.: Fractionation of hydrogen isotopes in lipid biosynthesis, Org. Geochem., 30(9), 1193-1200, 1999.

Sigman, D. M., Hain, M. P., Haug, G. H.: The polar ocean and glacial cycles in atmospheric CO2 concentration, Nature, 466, 47, 2010.

Simon, M. H., Ziegler, M., Bosmans, J., Barker, S., Reason, C. J. C., and Hall, I. R.: Eastern South African hydroclimate over the past 270,000 years, Sci. Rep., 5, 18153, https:doi.org /10.1038/srep18153, 2015.

Sonzogni, C., Bard, E., and Rostek, F.: Tropical sea-surface temperatures during the last glacial period: a view based on alkenones in Indian Ocean sediments, Quaternary Science Reviews, 17, 1185-1201, 1998.

Stager, J. C., Mayewski, P. A., White, J., Chase, B. M., Neumann, F. H., Meadows, M. E., King, C. D., and Dixon, D. A.: Precipitation variability in the winter rainfall zone of South Africa during the last 1400 yr linked to the austral westerlies, Climate of the Past Discussions, 7, 4375-4399, https:doi.org /10.5194/cpd-7-4375-2011, 2011.

Stuiver, M., Reimer, P., Reimer, R.: CALIB 7.1, http://calib.org, accessed 2019-8-23, 2019.

Sweeney, R. J., Duncan, A. R., Erlank, A. J.: Geochemistry and Petrogenesis of Central Lebombo Basalts of the Karoo Igneous Province, J. Petrol., 35(1), 95-125, 1994.

Tierney, J. E., Russell, J. M., Huang, Y., Damsté, J. S. S., Hopmans, E. C., and Cohen, A. S.: Northern Hemisphere Controls on Tropical Southeast African Climate During the Past 60,000 Years, Science, 322, 252-255, https:doi.org /10.1126/science.1160485, 2008.

Truc, L., Chevalier, M., Favier, C., Cheddadi, R., Meadows, M. E., Scott, L., Carr, A. S., Smith, G. F., and Chase, B. M.: Quantification of climate change for the last 20,000years from Wonderkrater, South Africa: Implications for the long-term dynamics of the Intertropical Convergence Zone, Palaeogeogr. Palaeoclimatol. Palaeoecol., 386, 575-587, https://doi.org/10.1016/j.palaeo.2013.06.024, 2013.

Tyson, P. D., Preston-Whyte, R. A.: Weather and climate of southern Africa, Oxford University Press., 2000.

Tyson, P. D.: The atmospheric modulation of extended wet and dry spells over South Africa, 1958–1978, Int. J. Climatol., 4, 621-635, https:doi.org /10.1002/joc.3370040606, 1984.

Walker, N. D.: Links between South African summer rainfall and temperature variability of the Agulhas and Benguela Current systems, J. Geophys. Res., 95(C3), 3297-3319, 1990.

Wang, Y. V., Leduc, G., Regenberg, M., Andersen, N., Larsen, T., Blanz, T., and Schneider, R. R.: Northern and southern hemisphere controls on seasonal sea surface temperatures in the Indian Ocean during the last deglaciation, Paleoceanogr., 28, 619-632, https:doi.org /10.1002/palo.20053, 2013.

White, F.,: The vegetation of Africa, Natural Resources Research, 20 UNESCO, Paris, 1983.

Xie, P., and Arkin, P. A.: Global precipitation: A 17-year monthly analysis based on gauge observations, satellite estimates, and numerical model outputs, Bull. Am. Meteorol. Soc., 78, 2539-2558, 1997.

Zabel, M.: Climate archives in coastal waters of southern Africa–Cruise No. M123–February 3–February 27, 2016–Walvis Bay (Namibia)–Cape Town (Rep. of South Africa), METEOR-Berichte M 123, 50, 2016.

Zhao, X., Dupont, L., Schefuß, E., Meadows, M., Hahn, A., and Wefer, G.: Holocene vegetation and climate variability between winter and summer rainfall zones of South Africa, Quat. Int., 404, 185-186, 2016.

Zahn, R., Hall, I., Schneider, R., Barker S., Compton, J., Dupont, L., Flores, J.-A., Franzese, A., Goldstein,S., Hemming, S., Knorr, G., Marino, G., Mazaud, A., Peeters, F., Preu, B., Reichert, G.-J., Spiess, V., Uenzelmann-Neben, G., Weldcab, S., Ziegler, M., 2012, Southern African Climates, Agulhas Warm Water Transports and Retroflection, and Interocean Exchanges - SAFARI: International Ocean Discovery Program.

Ziegler, M., Simon, M. H., Hall, I. R., Barker, S., Stringer, C., and Zahn, R.: Development of Middle Stone Age innovation linked to rapid climate change, Nat. Commun., 4, 1905, https:doi.org /10.1038/ncomms2897, 2013.

Table. 1 AMS radiocarbon analyses of material from core GeoB20616-1. The modelled ocean average curve (Marine13) (Reimer et al., 2013) was used for calibration and a local ΔR of 121±16 ^{14} C yr (Maboya et al. 2017) was applied. The ages were calibrated with Calib 7.1 software (Stuiver et al. 2018)

core	**material**	**depth (cm)**	**lab nur**	**^{14}C uncalib.**	**cal. age yrs BP -2s**	**+2s**	**median**
GeoB20616-1	bulk	0.5	Poz-89(	1640 ± 30 BP	972	1168	1075
GeoB20616-1	*Globigerinoides ruber*	2	Poz-88(	2860 ± 90 BP	2262	2718	2473
GeoB20616-1	*Globigerinoides ruber*	52	Poz-89(	5860 ± 150 BP	5794	5796	6139
GeoB20616-1	*Globigerinoides ruber*	102	Poz-89(	14290 ± 200 BF	16063	17248	16648
GeoB20616-1	*Globigerinoides ruber*	152	Poz-89(	13960 ± 390 BF	15047	17400	16170
GeoB20616-1	*Globigerinoides ruber*	202	Poz-89(	19160 ± 200 BF	22002	22971	22511
GeoB20616-1	*Globigerinoides ruber*	252	Poz-88(	20370 ± 220 BF	23342	24413	23877
GeoB20616-1	*Globigerinoides ruber*	302	Poz-89(	22070 ± 220 BF	25365	26216	25826
GeoB20616-1	*Globigerinoides ruber*	352	Poz-88(	30850 ± 870 BF	32455	36152	34343
GeoB 20616-1	shell fragment	390	Poz-85(	35820 ± 520 BF	38724	41007	39859
GeoB 20616-1	gastropod	634	Poz-85(	>52000 BP	Date out of range		
GeoB 20616 -1	coral	664	Poz-85(	>48000 BP	Date out of range		

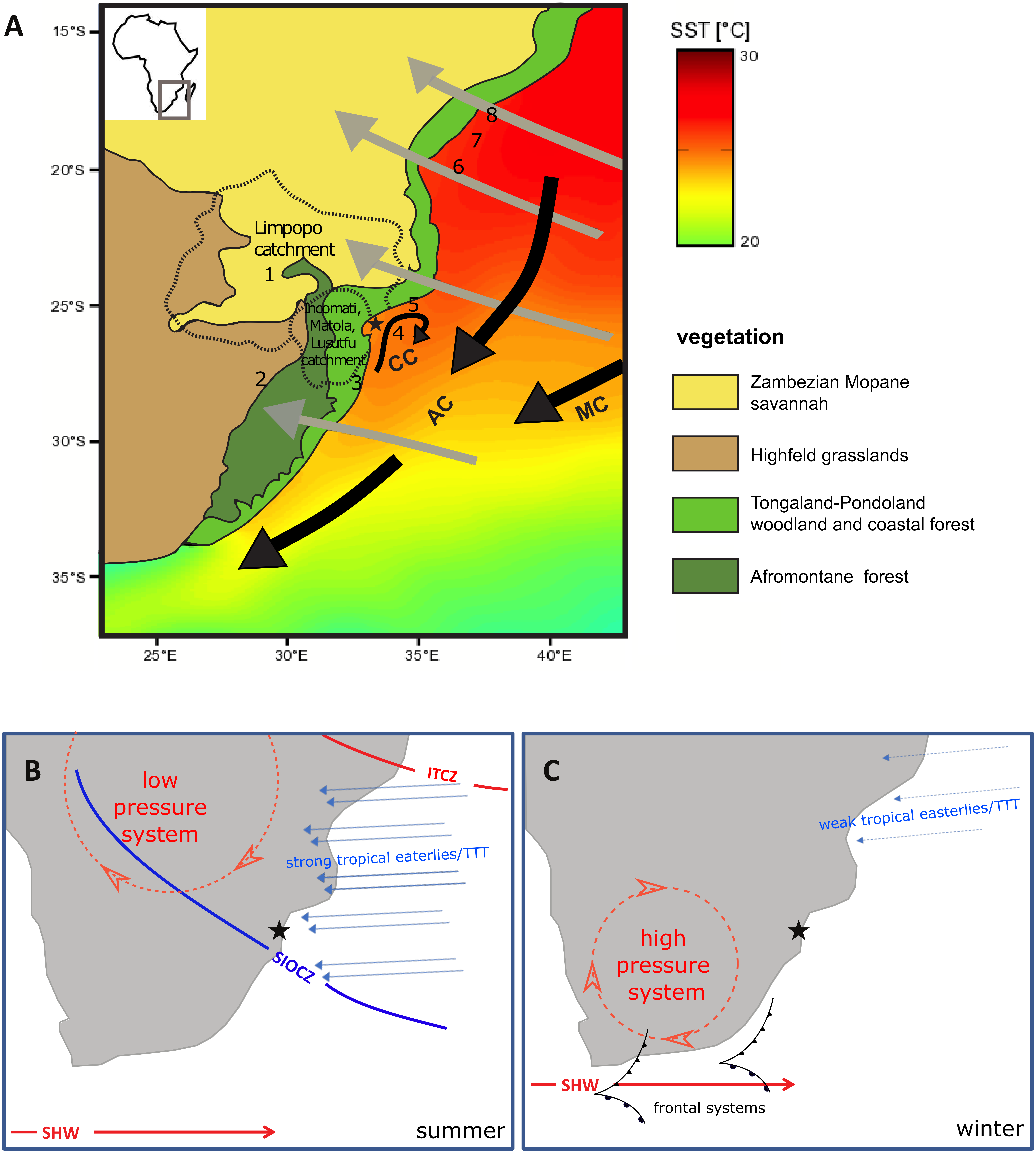
A
15°S
20°S
25°S
30°S
35°S
25°E
30°E
35°E
40°E
Limpopo catchment
1
2
3
4
5
6
7
8
Incomati, Matola, Lusutfu catchment
CC
AC
MC
SST [°C]
30
20
vegetation
Zambezian Mopane savannah
Highfeld grasslands
Tongaland-Pondoland woodland and coastal forest
Afromontane forest
B
low pressure system
ITCZ
strong tropical eaterlies/TTT
SIOCZ
SHW
summer
C
weak tropical easterlies/TTT
high pressure system
SHW
frontal systems
winter

Figure 2a)

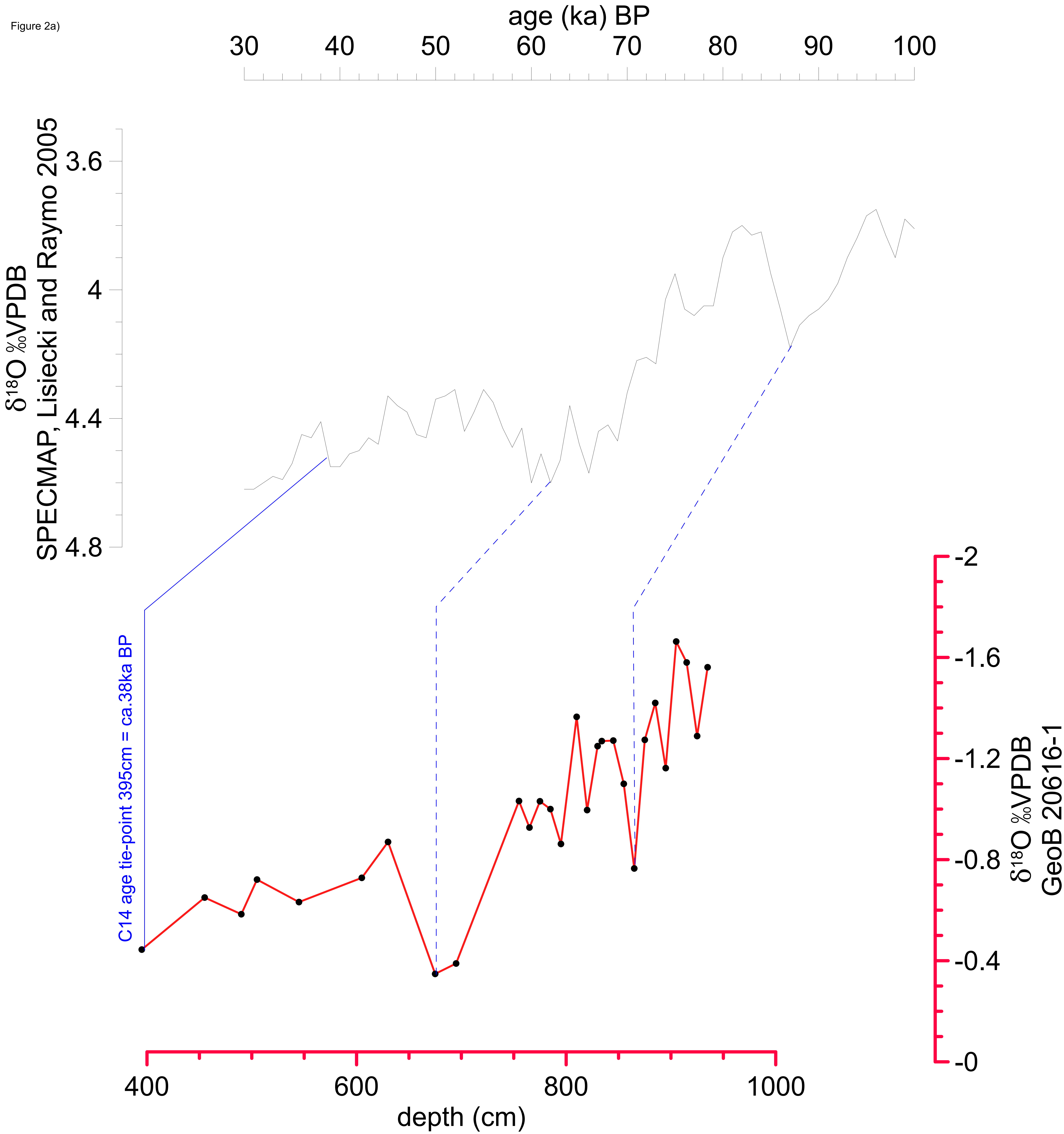
age (ka) BP
30
40
50
60
70
80
90
100
δ18O ‰VPDB
SPECMAP, Lisiecki and Raymo 2005
3.6
4
4.4
4.8
C14 age tie-point 395cm = ca.38ka BP
-2
-1.6
-1.2
-0.8
-0.4
-0
δ18O ‰VPDB
GeoB 20616-1
400
600
800
1000
depth (cm)

Figure 2b

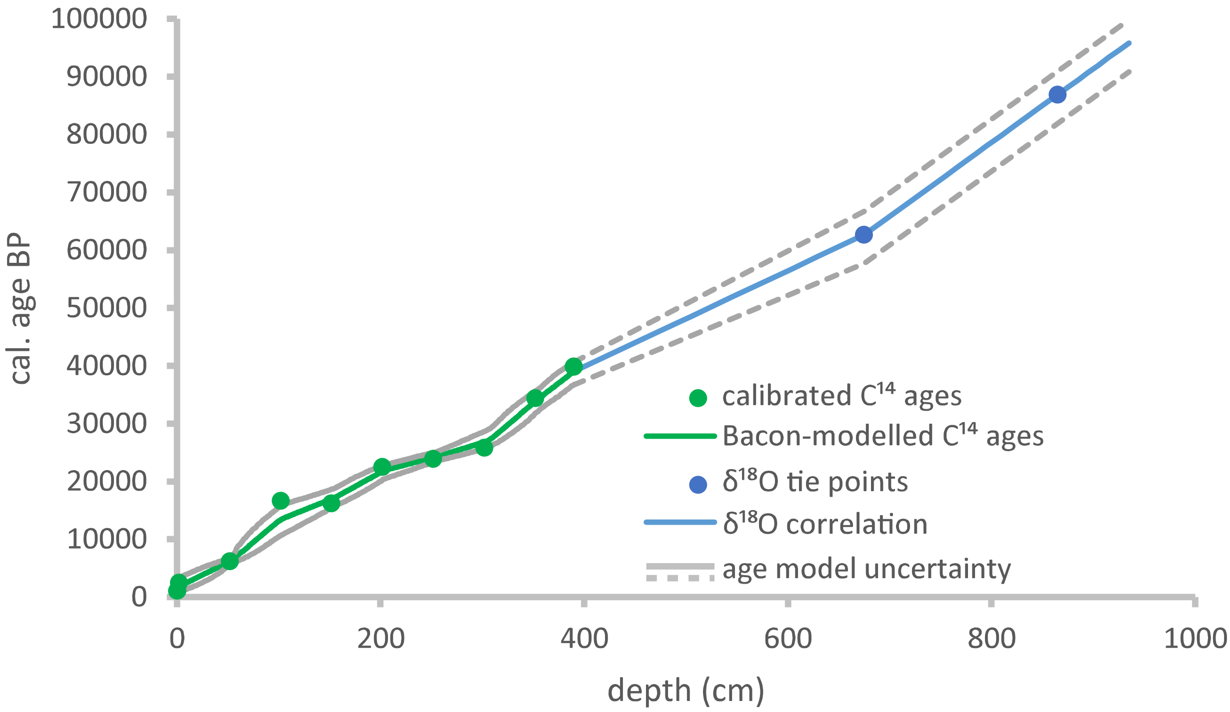

100000
90000
80000
70000
60000
50000
40000
30000
20000
10000
0
cal. age BP
0
200
400
600
800
1000
depth (cm)
calibrated C14 ages
Bacon-modelled C14 ages
δ18O tie points
δ18O correlation
age model uncertainty

Figure 3

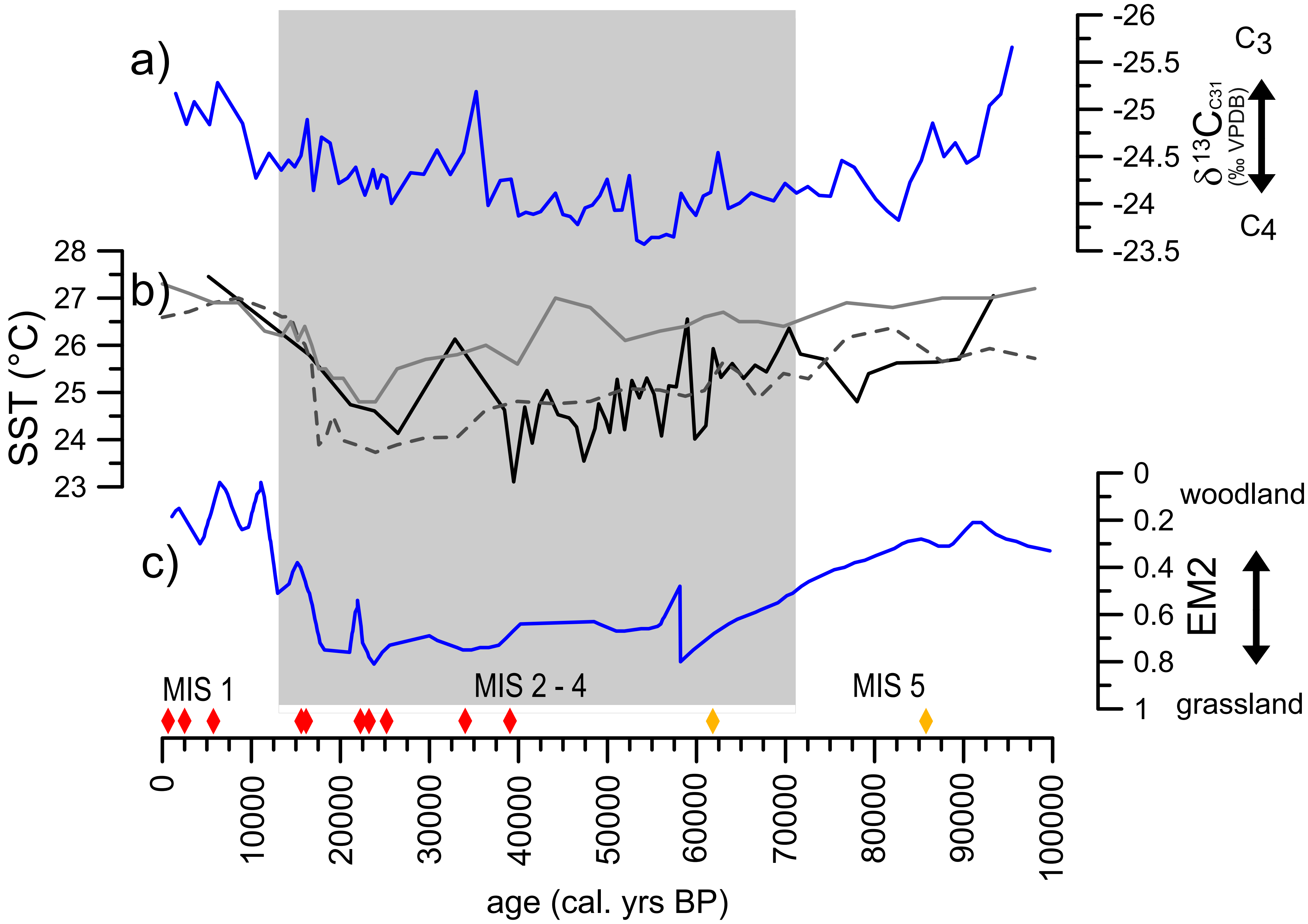

a)
b)
c)
-26
-25.5
-25
-24.5
-24
-23.5
C3
C4
δ13C C31 (‰ VPDB)
28
27
26
25
24
23
SST (°C)
0
0.2
0.4
0.6
0.8
1
woodland
grassland
EM2
MIS 1
MIS 2 - 4
MIS 5
0
10000
20000
30000
40000
50000
60000
70000
80000
90000
100000
age (cal. yrs BP)

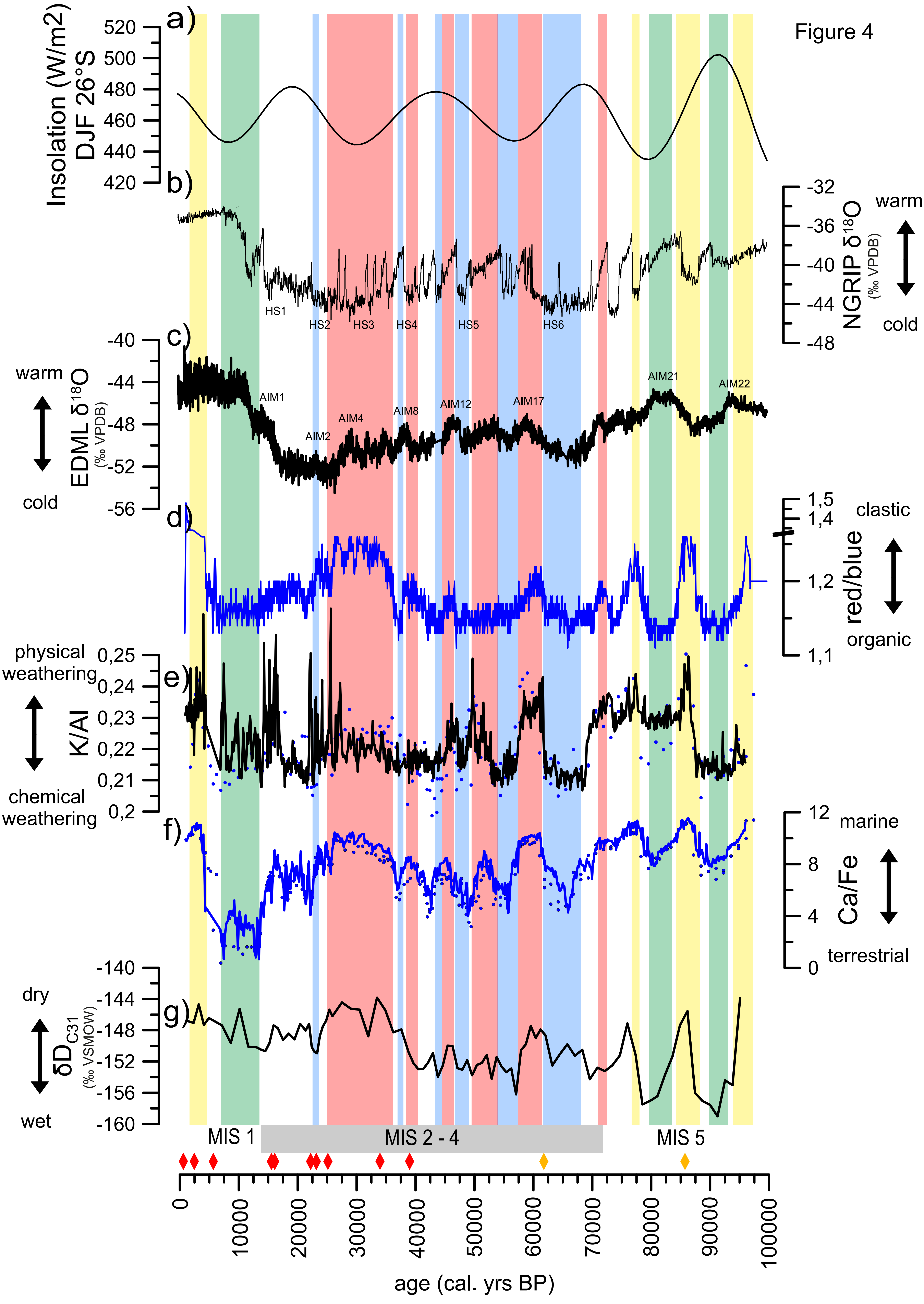

Figure 4
a)
Insolation (W/m2) DJF 26°S
520
500
480
460
440
420
b)
NGRIP δ18O (‰ VPDB)
-32
-36
-40
-44
-48
warm
cold
HS1
HS2
HS3
HS4
HS5
HS6
c)
EDML δ18O (‰ VPDB)
-40
-44
-48
-52
-56
warm
cold
AIM1
AIM2
AIM4
AIM8
AIM12
AIM17
AIM21
AIM22
d)
red/blue
1,5
1,4
1,2
1,1
clastic
organic
e)
K/Al
0,25
0,24
0,23
0,22
0,21
0,2
physical weathering
chemical weathering
f)
Ca/Fe
12
8
4
0
marine
terrestrial
g)
δD C31 (‰ VSMOW)
-140
-144
-148
-152
-156
-160
dry
wet
MIS 1
MIS 2 - 4
MIS 5
0
10000
20000
30000
40000
50000
60000
70000
80000
90000
100000
age (cal. yrs BP)

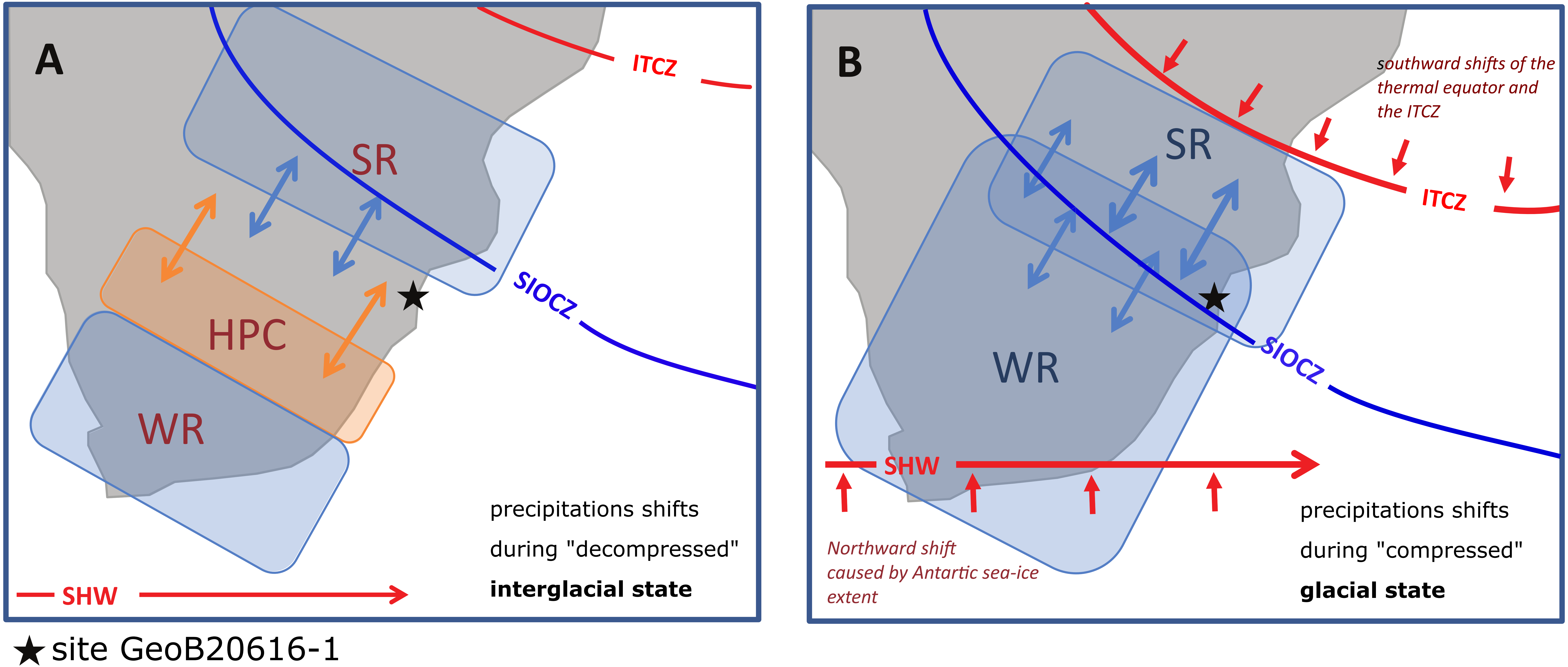
A
SR
HPC
WR
ITCZ
SIOCZ
SHW
precipitations shifts
during "decompressed"
interglacial state
B
SR
WR
ITCZ
SIOCZ
SHW
southward shifts of the
thermal equator and
the ITCZ
Northward shift
caused by Antartic sea-ice
extent
precipitations shifts
during "compressed"
glacial state
★ site GeoB20616-1

Supplement 1: GeoB20616-1 Oxygen and carbon isotopic composition of planktonic foraminifera.

age (cal. yrs BP)	**depth (cm)**	**$\delta^{18}O$ (‰ VPDB)**	**$\delta^{13}C$ (‰ VPDB)**
37173	395	-0.44	0.554
45285	455	-0.65	0.709
50017	490	-0.58	0.276
52045	505	-0.72	0.669
57453	545	-0.63	0.622
65565	605	-0.73	0.435
68945	630	-0.87	0.624
75029	675	-0.35	0.267
77733	695	-0.39	1.277
85845	755	-1.03	0.954
87197	765	-0.93	0.719
88549	775	-1.03	0.683
89901	785	-1.00	0.267
91253	795	-0.86	0.772
93281	810	-1.37	0.519
94633	820	-1.00	0.125
95985	830	-1.25	1.091
96525	834	-1.27	0.519
98013	845	-1.27	0.561
99365	855	-1.10	0.711
100717	865	-0.77	0.625
102069	875	-1.27	0.663
103421	885	-1.42	0.939
104773	895	-1.16	0.147
106125	905	-1.66	0.208
107477	915	-1.58	0.927
108829	925	-1.29	0.616
110181	935	-1.56	0.101

Supplement 2:GeoB20616-1 downcore sea surface temperatures (SST) calculated following Lea et al. 2003 using the listed ICP-OES measurement results.

age (cal. yrs BP)	depth (cm)	Mg/Ca	SST (°C)
5179	40.5	4.38	27.5
16512	145.5	3.77	25.8
21125	195.5	3.44	24.7
23832	245.5	3.40	24.6
26461	295.5	3.26	24.1
32869	345.5	3.89	26.1
38427	385.5	3.40	24.6
39467	395.5	2.97	23.1
40712	410.5	3.42	24.7
41542	420.5	3.20	23.9
42372	430.5	3.44	24.7
43202	440.5	3.53	25.0
44447	455.5	3.37	24.5
45692	470.5	3.35	24.5
46522	480.5	3.30	24.3
47352	490.5	3.09	23.5
48597	505.5	3.28	24.2
49012	510.5	3.44	24.8
49842	520.5	3.33	24.4
50258	525.5	3.26	24.2
51088	535.5	3.60	25.3
51918	545.5	3.28	24.2
52748	555.5	3.60	25.3
53578	565.5	3.48	24.9
54408	575.5	3.61	25.3
55238	585.5	3.50	25.0
56068	595.5	3.24	24.1
56898	605.5	3.56	25.1
57728	615.5	3.55	25.1
58973	630.5	4.04	26.6
59803	640.5	3.22	24.0
61048	655.5	3.30	24.3
61878	665.5	3.82	25.9
62748	675.5	3.62	25.3
64023	685.5	3.71	25.6
65298	695.5	3.61	25.3
66573	705.5	3.70	25.6
67848	715.5	3.66	25.4
69123	725.5	3.80	25.9
70397	735.5	3.97	26.4
71672	745.5	3.78	25.8
74222	765.5	3.74	25.7
78046	795.5	3.46	24.8
79321	805.5	3.64	25.4
82508	830.5	3.72	25.6
86970	865.5	3.72	25.6
89520	885.5	3.75	25.7
93344	915.5	4.22	27.1

Supplement 3: GeoB20616-1 organic geochemical down-core data. n-Alkane isotopic composition and distribution descriptive parameters averaged. The elevated CPI values ranging from 3.8 to 14 indicate that the *n* alkanes within the terrestrial and marine samples were likely derived from nondegraded, terrestrial, higher plant material (Eglinton & Hamilton, 1967). We focus the discussion on the isotopic signals of the *n* -C31 alkane but note that the *n* -C29 and *n* -C33 alkanes reveal similar trends.

age (cal. yrs BP)	Depth (cm)	$\delta^{13}C$-*n* C_{29} (‰ VPDB)	$\delta^{13}C$-*n* C_{31} (‰ VPDB)	$\delta^{13}C$-*n* C_{33} (‰ VPDB)	δD-*n* C_{29} (‰ VSMOW)	δD-*n* C_{31} (‰ VSMOW)	δD-*n* C_{33} (‰ VSMOW)	$CPI_{25\text{-}33}$
1504	2	-26.0	-25.2	-23.3	-133	-147	-150	6
2705	12	-25.6	-24.8	-23.2	-140	-147	-150	6
3580	22	-26.2	-25.1	-23.3	-138	-145	-148	7
4442	32	-26.1	-25.0	-23.2	-144	-147	-151	7
5306	42	-26.0	-24.8	-23.0	-130	-146	-148	7
6197	52	-25.7	-25.3	-23.2				7
7535	62				-140	-147	-148	7
9007	72	-25.9	-24.9	-23.0	-137	-150	-150	8
10513	82	-25.2	-24.3	-22.5	-134	-145	-149	7
11985	92	-24.9	-24.5	-22.4	-136	-150	-151	8
13363	102	-25.1	-24.4	-22.5	-141	-150	-151	7
14163	112	-25.2	-24.5	-22.6	-136	-150	-150	7
14871	122	-25.2	-24.4	-22.5	-145	-151	-151	8
15571	132	-25.4	-24.5	-22.7	-135	-150	-149	7
16271	142	-25.5	-24.9	-22.8	-141	-147	-147	7
16979	152	-24.8	-24.1	-22.2	-139	-148	-145	7
17878	162	-25.0	-24.7	-22.6	-143	-149	-149	8
18839	172	-25.2	-24.6	-22.6	-135	-148	-149	7
19822	182	-24.9	-24.2	-22.3	-138	-149	-151	7
20787	192	-25.0	-24.3	-22.4	-139	-147	-147	7
21724	202	-25.1	-24.4	-22.5	-138	-148	-148	7
22300	212	-25.0	-24.2	-22.4	-130	-147	-148	7
22756	222	-24.7	-24.1	-22.2	-137	-150	-150	11
23217	232	-25.0	-24.2	-22.4	-135	-151	-149	8
23673	242	-25.5	-24.4	-22.5	-135	-151	-150	7
24131	252	-24.7	-24.2	-22.3	-132	-149	-148	7
24642	262	-25.3	-24.3	-22.5	-132	-148	-148	7
25187	272	-25.4	-24.3	-22.4	-131	-147	-148	7
25731	282	-25.0	-24.0	-22.3	-135	-145	-149	7
26273	292				-138	-146	-148	8
27880	312	-25.2	-24.3	-22.4	-138	-144	-148	7
29364	322	-25.4	-24.3	-22.6	-130	-145	-147	7
30853	332	-25.4	-24.6	-22.6	-132	-145	-147	7
32351	342	-25.3	-24.3	-22.5	-142	-149	-151	7
33833	352	-25.5	-24.5	-22.6	-127	-144	-147	7
35256	362	-25.9	-25.2	-23.2	-141	-145	-150	8
36591	372	-25.1	-24.0	-22.1	-133	-148	-152	8
37949	382	-25.1	-24.2	-22.3	-132	-148	-149	7
39177	392	-25.0	-24.3	-22.6	-143	-151	-153	7
40007	402	-24.9	-23.9	-22.2	-137	-152	-152	8
40837	412	-24.8	-23.9	-22.1	-143	-153	-155	7
41667	422	-24.8	-23.9	-22.0	-144	-153	-153	8
42497	432	-24.9	-23.9	-22.1	-142	-152	-154	8
43327	442	-25.0	-24.0	-22.2	-136	-151	-152	7
44157	452	-25.3	-24.1	-22.4	-138	-154	-154	7
44987	462	-24.9	-23.9	-22.2	-137	-153	-154	7
45817	472	-25.0	-23.9	-22.0	-143	-150	-152	7
46647	482	-24.7	-23.8	-22.0	-145	-150	-152	6
47477	492	-25.0	-24.0	-22.1	-138	-153	-154	7
48307	502	-24.7	-24.0	-22.1	-142	-153	-153	7
49137	512	-25.0	-24.1	-22.1	-145	-152	-153	7
49967	522	-24.9	-24.3	-22.2	-143	-154	-155	7
50797	532	-24.9	-23.9	-22.0	-142	-152	-154	7
51627	542	-24.9	-23.9	-22.1	-141	-152	-155	6
52457	552	-24.1	-24.3	-22.7	-139	-151	-154	7
53287	562	-24.7	-23.6	-22.0	-141	-154	-155	9
54117	572	-24.4	-23.6	-21.9	-137	-151	-153	7
54947	582	-24.6	-23.6	-22.1	-147	-153	-154	7
55777	592	-24.3	-23.6	-22.0	-147	-153	-155	7
56607	602	-24.8	-23.7	-21.9	-138	-153	-155	6
57437	612	-24.7	-23.6	-22.1	-147	-156	-156	7
58267	622	-25.1	-24.1	-22.3	-145	-151	-152	7
59097	632	-25.1	-24.0	-22.3	-138	-150	-152	7
59927	642	-25.0	-23.9	-22.1	-134	-147	-148	6
60757	652	-25.1	-24.1	-22.4	-139	-149	-148	7
61588	662	-25.1	-24.1	-22.4	-136	-148	-149	7
62418	672	-25.4	-24.5	-22.8	-132	-149	-148	7
63577	682	-25.4	-23.9	-22.5	-146	-153	-153	8
64852	692	-24.8	-24.0	-22.4	-134	-151	-152	7
66127	702	-25.0	-24.1	-22.6	-134	-150	-151	7
67402	712	-24.8	-24.1	-22.5	-134	-151	-153	7
68676	722	-25.1	-24.0	-22.6	-144	-151	-152	7
69951	732	-25.3	-24.2	-22.8	-138	-154	-156	7
71226	742	-25.6	-24.1	-22.7	-138	-153	-155	7
72501	752	-25.4	-24.2	-22.6	-138	-153	-156	7
73776	762	-25.4	-24.1	-22.6	-140	-152	-153	7
75050	772	-25.4	-24.1	-22.6	-145	-151	-153	7
76325	782	-26.3	-24.5	-23.0	-137	-147	-150	6
77728	793	-25.8	-24.4	-22.7	-142	-151	-154	8
78875	802	-25.2	-24.2	-22.3	-153	-157	-159	7
80150	812	-25.3	-24.0	-22.3	-137	-157	-159	6
81425	822	-25.3	-23.9	-22.3	-149	-156	-159	6
82699	832	-24.0	-23.8	-22.2	-137	-154	-155	5
83974	842	-25.5	-24.2	-22.6	-144	-151	-153	6
85249	852	-25.6	-24.5	-22.8	-141	-147	-152	7
86524	862	-26.2	-24.9	-23.1	-142	-146	-151	1
87799	872	-25.9	-24.5	-22.8	-146	-156	-157	6
89074	882	-26.2	-24.6	-22.9	-147	-157	-157	6
90348	892	-25.8	-24.4	-22.7	-151	-158	-161	7
91623	902	-26.1	-24.5	-22.9	-150	-159	-160	6
92898	912	-26.4	-25.0	-22.9	-139	-154	-157	7
94173	922	-26.6	-25.2	-23.1	-141	-155	-158	7
95448	932	-26.3	-25.7	-23.6	-134	-144	-146	7

Supplement 4: GeoB20616-1 inorganic geochemical down-core data from

depth (cm)	age (cal. years BP)	Al (mg/kg)	Ca (mg/kg)	Fe (mg/kg)	K (mg/kg)
5.5	2141	41601	177248	27139	8911
10.5	2575	40009	184378	26882	8863
15.5	3008	33894	202638	23765	8045
20.5	3446	32489	209794	22430	7864
25.5	3891	42712	174836	30180	10010
30.5	4315	51353	145437	36638	11646
35.5	4741	52964	143556	38025	12066
40.5	5179	61319	114217	41607	13549
45.5	5600	62755	114701	43780	13466
50.5	6032	76367	67954	51567	15949
55.5	6602	64118	106827	43037	13586
60.5	7317	81808	55271	53594	16917
65.5	8040	78369	59242	50854	16399
70.5	8781	75738	70803	48374	15809
75.5	9523	78203	60655	52427	16661
80.5	10290	78352	59011	51635	16528
85.5	11035	77321	59370	54169	16743
90.5	11767	76465	63916	55399	16351
95.5	12501	75170	61400	53243	16427
100.5	13211	77240	61674	55229	16505
105.5	13696	74527	68091	55522	16528
110.5	14057	74176	67078	52330	15914
115.5	14409	71905	75806	48928	15316
120.5	14766	68726	82184	47674	15031
125.5	15118	64537	95917	45311	13962
130.5	15468	61688	99668	41571	13308
135.5	15813	59928	106381	41391	13475
140.5	16168	62339	102200	42106	13815
145.5	16512	53917	124124	38125	12401
150.5	16868	53583	129426	38349	12385
155.5	17255	62403	104697	43747	13950
160.5	17734	66270	88069	48473	14453
165.5	18215	56286	115156	39825	13046
170.5	18696	67792	80244	44942	14654
175.5	19176	66981	88478	45807	14197
180.5	19674	62491	95931	42658	13873
185.5	20162	65334	99870	47296	14113
190.5	20643	62511	102887	41707	13467
195.5	21125	66868	96885	48235	14988
200.5	21597	67068	89420	49711	15021
205.5	22000	69028	90573	44979	14341
210.5	22233	60283	114739	42526	13499
215.5	22458	69104	88862	45349	14645
220.5	22687	70456	88409	45770	14638
225.5	22917	72078	84770	46615	14792
230.5	23146	65131	103541	43173	13557
235.5	23379	56941	129414	38257	12407
240.5	23605	60846	120300	40670	12692
245.5	23832	57609	129981	41183	12521
250.5	24063	58536	123484	41087	12795
255.5	24298	58042	123364	40032	12580
260.5	24562	57797	129772	43387	13060
280.5	25648	60102	118404	40438	13120
285.5	25922	59111	122979	41101	12896
290.5	26193	60619	123278	41523	12833
295.5	26461	48348	167591	34485	10447
300.5	26733	44819	174138	31605	10008
305.5	27045	44879	172727	32203	10102
310.5	27652	45798	169598	32696	10287
315.5	28407	51376	146621	36184	11618
320.5	29142	45342	164907	31759	10547
325.5	29884	54584	140547	36636	12082
330.5	30625	49338	155126	34580	11003
335.5	31378	49564	154649	34299	11218
340.5	32130	52464	140437	37184	11815
345.5	32869	53070	137093	36736	11702
350.5	33615	53940	137642	38276	12143
355	34273	55917	113821	35189	12547
355.5	34346	56963	129853	40731	12948
360	34982	56742	111906	36524	12790
360	34982	51631	124407	35717	11300
360.5	35050	57729	127739	40217	12990
365	35663	55346	112114	34237	12311
365.5	35731	56217	128293	39866	12775
370	36319	52984	117699	35315	11500
370	36319	54704	116866	36474	12137
370.5	36386	57846	110492	39138	13301
375.5	37069	66718	83800	46061	14718
380	37677	66930	72739	41065	14458
380	37677	64675	79088	44574	13757
380.5	37744	65197	85613	44766	14634
385.5	38427	64755	94671	44168	14123
390	39011	63041	93578	42042	12755
390.5	39052	64839	97063	45540	13991
395.5	39467	64293	101333	43352	13659
400	39841	56336	111917	37771	11815
400.5	39882	59540	116418	40174	12958
405	40256	60525	101730	35780	13075
405.5	40297	60053	113436	41620	13286
410	40671	56134	111014	37702	11909
410.5	40712	61267	115181	40783	13059
415.5	41127	68070	96946	45136	14410
420	41501	60132	92248	41222	12966
420.5	41542	63673	107364	44591	13908
425	41916	64280	79834	42446	14274
425.5	41957	67059	90673	43957	14495
430	42331	66538	74768	44034	13772
430.5	42372	74425	72721	49023	16000
435	42746	68276	73664	46167	14581
435.5	42787	74586	74830	48272	15428
440	43161	68894	68864	42636	13686
440.5	43202	73481	85417	52971	15420
445	43576	63726	90121	43258	13714
445.5	43617	70805	90745	47880	14455
450	43991	62794	94709	41966	12541

450.5	44032	66645	102400	44605	14024
455.5	44447	63058	110000	43305	13270
460	44821	60234	103253	41532	12445
460	44821	63467	94432	41145	13774
460.5	44862	66633	99157	45814	14019
465.5	45277	63091	106734	43179	13627
470	45651	58903	94189	39768	12457
470.5	45692	63933	103868	45098	14305
475	46066	60994	86668	37042	13787
475.5	46107	61837	98873	41100	14153
480	46481	56561	90832	40272	12613
480.5	46522	66192	89069	45694	14571
485.5	46937	67609	86077	46304	14804
490	47311	62425	78589	42526	13456
490.5	47352	73996	74298	50343	15312
495	47726	63854	82115	42127	14185
495.5	47767	70040	79558	47674	14918
500	48141	58443	92436	39597	12792
500.5	48182	67806	89654	41300	14255
505.5	48597	64302	95964	42143	13817
510	48971	56298	89156	36482	12774
510.5	49012	58933	107154	37850	13198
515.5	49427	56637	121832	39000	13166
520	49801	69152	66613	44369	14418
520.5	49842	61249	102619	40085	14223
525.5	50258	59082	98837	38056	13993
530	50631	63717	71262	40987	13969
530.5	50673	62272	86967	41175	14570
535.5	51088	66636	77489	41972	15207
540	51461	67956	65810	40760	14770
540.5	51503	68530	79364	46688	15272
545.5	51918	71167	71372	47010	16052
550.5	52333	69486	77430	47457	15274
555.5	52748	73000	67616	47939	15957
560	53121	70124	57144	42084	15288
560	53121	65831	79730	43561	13966
560.5	53163	70140	86254	47706	15075
565.5	53578	72087	78510	46632	15068
570	53951	66312	82360	42526	14264
570	53951	66194	76845	43042	13921
580	54781	66247	80417	44078	14268
580	54781	68014	77544	46462	13950
590	55611	66355	83582	44236	14347
590	55611	65058	82253	45714	13717
600	56441	61234	89130	40404	13039
610	57271	55032	110938	38905	12495
610	57271	58564	100873	40606	12782
620	58101	45455	139095	31370	10910
620	58101	44378	145060	31074	10138
625	58516	43060	142267	29805	10433
630	58931	42528	144291	29578	9941
635	59346	42342	162679	30808	10345
640	59761	43435	145528	30639	10129
645	60176	43778	146212	29584	10425
650	60591	42732	148481	29140	10062
660	61422	51553	125405	35513	11277
670	62252	61084	96695	42103	12882
670	62252	64483	93359	45537	13816
680	63322	67129	77902	46161	14021
680	63322	62970	93170	43272	13659
690	64597	67932	76483	44205	13923
690	64597	68020	73796	46466	14663
700	65872	67826	80960	48905	14043
710	67147	58768	103678	40525	12421
710	67147	62192	95677	50634	13671
720	68421	62300	100698	43941	13308
720	68421	59517	102095	41114	12571
730	69696	51990	130019	36401	11173
730	69696	60917	103143	43866	13069
740	70971	42149	152024	32335	9772
740	70971	48978	143668	38215	11380
750	72246	48501	141805	34406	11020
760	73521	45861	150455	33980	10725
760	73521	47125	143183	34141	10539
770	74795	42528	162159	31551	10067
770	74795	39344	169696	30045	9127
780	76070	34419	192887	25895	8236
780	76070	31427	202857	23010	7502
790	77345	35777	183667	26151	8677
790	77345	35244	183499	24784	8237
800	78620	51577	132777	38252	11201
810	79895	55158	111085	40599	11873
820	81170	50305	125661	37449	11178
825	81807	52630	126976	38524	12155
830	82444	48311	141565	35482	10618
835	83082	48136	145329	35219	11257
840	83719	47482	150996	34356	10533
850	84994	32646	192928	21969	7706
860	86269	22912	239594	17648	5737
860	86269	26057	230951	18877	6348
870	87544	28890	213965	20328	6753
870	87544	52404	134379	37382	11542
880	88819	62396	105431	42914	13482
880	88819	57738	112182	39138	11802
890	90093	54070	123836	39282	11467
890	90093	61059	108961	41761	13009
900	91368	63645	102706	44565	13416
900	91368	62597	112688	41009	13450
910	92643	61222	107700	40574	12949
910	92643	62867	108253	42496	13677
920	93918	55146	133032	37836	11767
920	93918	55676	134602	38464	12232
930	95193	51392	139805	33200	11087
930	95193	50522	153534	33390	11269
940	96468	44837	163431	28193	9756
940	96468	22365	244843	14395	5517
950	97742	21712	244971	13257	5156